Spring photosynthetic onset and net CO2 uptake in Alaska triggered by landscape thawing

Parazoo, Nicholas; Arneth, Almut; Pugh, Thomas; Smith, Benjamin; Steiner, Nicholas; Luus, Kristina; Commane, Roisin; Benmergui, Josh; Stofferahn, Eric; Liu, Junjie; Rödenbeck, Christian; Kawa, Randy; Euskirchen, Eugenie; Zona, Donatella; Arndt, Kyle; Oechel, Walt; Miller, Charles

Document Version
Peer reviewed version

Citation for published version (Harvard):
Parazoo, N, Arneth, A, Pugh, T, Smith, B, Steiner, N, Luus, K, Commane, R, Benmergui, J, Stofferahn, E, Liu, J, Rödenbeck, C, Kawa, R, Euskirchen, E, Zona, D, Arndt, K, Oechel, W & Miller, C 2018, 'Spring photosynthetic onset and net CO2 uptake in Alaska triggered by landscape thawing' Global Change Biology. https://doi.org/10.1111/gcb.14283

[Link to publication on Research at Birmingham portal](#)

1

2

3

Spring photosynthetic onset and net CO₂ uptake in Alaska triggered by landscape thawing

Nicholas Parazoo[1], Almut Arneth[2], Thomas Pugh[3,4], Ben Smith[5], Nicholas Steiner[6], Kristina Luus[7], Roisin Commane[8], Josh Benmergui[8], Eric Stofferahn[9], Junjie Liu[1], Christian Rödenbeck[10], Randy Kawa[11], Eugenie Euskirchen[12], Donatella Zona[13], Kyle Arndt[13], Walt Oechel[13], Charles Miller[1]

Jet Propulsion Laboratory, California Institute of Technology[1]

Institute of Meteorology and Climate Research (IMK-IFU), Karlsruhe Institute of Technology, Garmisch-Pertenkirchen, Germany[2]

School of Geography, Earth and Environmental Sciences, University of Birmingham, UK.[3]

Birmingham Institute of Forest Research, University of Birmingham, U.K.[4]

Department of Physical Geography and Ecosystem Science, Lund University[5]

Department of Earth and Atmospheric Sciences, The City College of New York[6]

Centre for Applied Data Analytics, Dublin, Ireland[7]

Department of Earth and Planetary Sciences, Harvard University[8]

Conservation Science Partners, Truckee, CA[9]

Max Plank Institute for Biogeochemistry[10]

NASA Goddard Space Flight Center[11]

Institute of Arctic Biology, University of Alaska Fairbanks[12]

Biology Department, San Diego State University[13]

Prepared for Global Change Biology

31 **Abstract**

32 The springtime transition to regional-scale onset of photosynthesis and net ecosystem carbon

33 uptake in boreal and tundra ecosystems is linked to the soil freeze-thaw state. We present

34 evidence from diagnostic and inversion models constrained by satellite fluorescence and airborne

35 CO_2 from 2012-2014 indicating the timing and magnitude of spring carbon uptake in Alaska

36 correlates with landscape thaw and ecoregion. Landscape thaw in boreal forests typically occurs

37 in late April (DOY 111±7) with a 29±6 day lag until photosynthetic onset. North Slope tundra

38 thaws 3 weeks later (DOY 133±5) but experiences only a 20±5 day lag until photosynthetic

39 onset. These time lag differences reflect efficient cold season adaptation in tundra shrub, and the

40 longer dehardening period for boreal evergreens. Despite the short transition from thaw to

41 photosynthetic onset in tundra, synchrony of tundra respiration with snowmelt and landscape

42 thaw delays the transition from net carbon loss (at photosynthetic onset) to net uptake by 13±7

43 days, thus reducing the tundra net carbon uptake period. Two global CO_2 inversions using a

44 CASA-GFED model prior estimate earlier northern high latitude net carbon uptake compared to

45 our regional inversion, which we attribute to (1) early photosynthetic onset model prior bias, (2)

46 inverse method (scaling factor + optimization window), and (3) sparsity of available Alaskan

47 CO_2 observations. Another global inversion with zero prior estimates the same timing for net

48 carbon uptake as the regional model but smaller seasonal amplitude. Analysis of Alaskan eddy

49 covariance observations confirms regional scale findings for tundra, but indicates that

50 photosynthesis and net carbon uptake occur up to 1 month earlier in evergreens than captured by

51 models or CO_2 inversions, with better correlation to above-freezing air temperature than date of

52 primary thaw. Further collection and analysis of boreal evergreen species over multiple years and

53 at additional sub-Arctic flux towers is critically needed.

54

Introduction

The future trajectory of the Arctic Boreal Zone as a net carbon (C) sink or source is of global importance due to vast quantities of C stored in permafrost (Hugelius et al., 2014). Climate warming threatens to thaw and release permafrost C back to the atmosphere as the greenhouse gases carbon dioxide (CO_2) and methane, creating a positive feedback and promoting further global warming (Hinzman et al., 2013). At the same time, warming can lead to higher productivity (Natali et al., 2012), creating temporary C sinks via increased above-ground biomass and delayed decomposition, offsetting potential C losses. The remainder of this paper focuses on C in the form of CO_2.

The balance of net ecosystem C gain and loss processes is strongly modulated by land surface freeze/thaw dynamics, the timing and duration of seasonal soil thawing (defined as the transition from frozen to unfrozen soil water state), vegetation growing season, and surface moisture supply (Kim et al., 2014; Yi et al., 2014). In spring, plant productivity (denoted as gross primary production, or GPP) is hindered by cold temperatures and lack of liquid water in frozen soils and snow cover. Climate warming promotes earlier landscape thawing (Goulden, 1998), reduced spring snow cover duration (Lawrence & Slater, 2010), earlier budburst (Badeck et al., 2004), and longer growing seasons (Barichivich et al., 2013). These processes lead to higher GPP through simultaneous warming, CO_2 fertilization, and increased woody biomass (Bhatt et al., 2010; Elmendorf et al., 2012; McGuire et al., 2012). Earlier spring snow melt and thawing also expose the land surface to increasing solar absorption resulting in a longer decomposition season, active layer deepening, an extended zero curtain period and talik formation, which can stimulate terrestrial ecosystem respiration (TER) through enhanced soil warming and water drainage (Lawrence et al., 2008; Romanovsky & Osterkamp, 2000).

The impacts of changes in growing season length on annual C balance are not well modeled (Schaefer et al., 2012). In particular, Earth System Models used in IPCC climate assessments predict photosynthetic growing season onsets that are systematically early on local (Peng et al., 2015) to regional scales (Commane et al., 2017a). In turn, GPP biases propagate through the model and affect the timing and magnitude of estimated net biosphere production (NBP) (Wang et al., 2012), representing the balance of GPP and TER (NBP = GPP – TER). Because climate change at high latitudes promotes earlier and longer growing seasons (Barichivich et al., 2013;

85 Kim et al., 2012), while the photoperiod remains fixed, models with early spring bias in the

86 current climate are likely to under-estimate the photosynthetic response to future warming.

87 Consequently, errors in the simulation of growing season onset and duration provide a plausible

88 explanation for the tendency of Earth System Models to underestimate peak growing season C

89 uptake in response to climate warming (Graven et al., 2013).

90 It is well known that changes in spring GPP onset in cold northern latitudes corresponds closely

91 with changes in the date of soil thaw when liquid water becomes available (Troeng and Linder,

92 1982; Black et al., 2000; Goulden, 1998; Jarvis & Linder, 2000). In evergreen needleleaf forests

93 (denoted evergreens), assimilated C initially accumulates as starch following soil thaw, and then

94 is used to grow new foliage, branches, and stem during the growing season peak (Bergh et al.,

95 1998). GPP onset can occur several weeks prior to changes in biomass in conifers (Ottander et

96 al., 1995; Soukupova et al., 2008; Richardson et al., 2011), but the spring dehardening period,

97 during which plants undergo the biochemical changes needed for green-up, can slow recovery

98 from winter dormancy (Ensminger et al., 2008). Land surface models that do not account for

99 effects of frozen soils or recovery of photosynthetic capacity in spring and summer overestimate

100 GPP gain by up to 10% across the entire permafrost domain (Jafarov & Schaefer, 2016) and up

101 to 40% in boreal forests (Bergh et al., 1998). However, the relationship between spring GPP

102 onset and soil freeze/thaw is complicated by confounding air temperature and snow cover

103 effects, which can lead to GPP onset while soils are frozen (Esminger et al., 2004; Arneth et al.,

104 2006; Jonsson et al., 2010; Gonsamo et al., 2012; Walther et al., 2016; Pulliainen et al., 2017).

105 Tundra ecosystems in the far northern Alaskan and Siberian Arctic also show a pattern of

106 increased GPP and NBP in spring with warming and earlier soil thaw and snowmelt (Griffis et

107 al., 2000; Harazono et al., 2003; Arneth et al., 2006; Lafleur et al., 2007; Ueyama et al., 2013).

108 The length of time from soil thaw to onset of GPP and net C uptake (date when ecosystem shifts

109 from net C source to net sink), however, varies under different environmental conditions and

110 vegetation types. Simultaneous increases in soil respiration (i.e., TER) with GPP following thaw

111 and snowmelt can delay daily net C uptake by 5-23 days depending on ambient temperature

112 (Oberbaur et al., 1998; Lafleur et al., 2007). Ecosystem type and fraction of evergreen vs

113 deciduous species is also important. Multi-year observations from a cluster of flux towers on the

114 Alaskan North Slope show much stronger correlation of thaw date with heath and wet sedge

tundra than with tussock tundra (Euskirchen et al., 2017). Likewise, evergreen mosses and lichens transition to net uptake within one week of snowmelt, while deciduous shrubs show a slower transition of 1-3 weeks (Lafleur et al., 2007). Direct observations of *Sphagnum* (moss) along the northern coast of Alaska, near Barrow, show very weak levels of initial photosynthesis following snowmelt due to photoininhibition as a stress response to high radiation levels, causing a delay in net C uptake of ~3 weeks (Zona et al., 2011). The exact timing of spring GPP onset and transition to net C uptake in Arctic tundra and in boreal ecosystems is thus not well established at regional scale, in part due to sparse and variable results from field measurements, but also because reliable indicators of GPP onset are limited.

Solar induced chlorophyll fluorescence (SIF) measures a direct outcome of foliar light absorption by chlorophyll and provides an important seasonal GPP proxy (Frankenberg et al., 2011; Parazoo et al., 2014). Recent satellite SIF estimates have been used to accurately represent the timing of spring GPP onset and the duration of growing season C uptake in Alaskan ecosystems (Walther et al., 2016; Jeong et al., 2017; Luus et al., 2017; Commane et al., 2017a). In particular, Luus et al. (2017) show greenup and budburst to occur 1-2 weeks prior to SIF based GPP onset in northern high latitude deciduous tundra ecosystems. Moreover, leaf level SIF measurements show close correspondence to photochemical reflectance index and chlorophyll carotenoid index optical indices during spring photosynthetic activation (from gas exchange measurements) in boreal evergreens, reflecting a reversal of non-photochemical quenching and leaf pigments in spring with changes in chloroplast functioning during cold dehardening (Wong & Gamon, 2015; Springer et al., 2017). Especially in evergreens, SIF remote sensing has potential to provide a powerful measure of the reactivation of photosynthesis in spring at large spatial scales, which is otherwise invisible and difficult to assess with reflectance-based optical indices (Wong and Gamon, 2015; Walther et al., 2016).

Analysis of SIF-GPP relationships in Alaska has shed light on the effects of plant structural vs functional phenology changes on seasonal C fluxes across key Arctic biomes, and helped quantify Alaskan C balance (Commane et al., 2017a), but have not yet clarified links between plant phenology and environmental effects in driving seasonal onset of GPP and net C uptake. As such, our quantitative and mechanistic understanding of links between environmental forcing, phenology response, and plant C uptake across tundra and boreal ecosystems requires further

145 refining, and improved estimates of the timing of thaw, GPP, and net C uptake at regional-scale.

146 Here, we establish empirical relationships between spring thaw, GPP onset, and net C uptake at

147 regional scale as derived from established GPP and NBP estimates constrained by satellite

148 fluorescence and airborne CO_2 observations in Alaska (Luus et al., 2017; Commane et al.,

149 2017a). We also analyze regional estimates against eddy covariance observations at boreal and

150 tundra sites in interior and North Slope Alaska. By quantifying these relationships, we seek to

151 determine the extent to which landscape thaw controls the timing of GPP and net C uptake onset

152 in northern ecosystems, and understand the ecosystem dependencies and physiological

153 mechanism behind the timing and time lag of thaw and C fluxes.

154

155 **Materials and Methods**

156 *Freeze/Thaw State Determination*

157 Daily 10-km resolution maps of the bulk freeze/thaw state of the Alaskan land surface were

158 determined for 2012-2014 using passive microwave observations from the Advanced Microwave

159 Scanning Radiometer-EOS (AMSR-E) and the Special Sensor Microwave Imager/Sounder

160 (SSMIS-F17). The freeze/thaw mapping algorithm is based on wavelet analysis, which uses a

161 time-series singularity classifier to identify the timing of freeze/thaw and snowmelt transitions

162 (Steiner & Tedesco, 2014; Steiner et al., 2015; 2017). A brightness temperature gradient ($K - K_a$

163 Bands), sensitive to transitions between frozen and liquid state of water caused by contrasts in

164 the bulk landscape complex dialectric constant, is used to determine freeze/thaw status (Zhang &

165 Armstrong, 2001). Peak diurnal difference brightness temperatures determine snowmelt status

166 (Ramage & Isacks, 2002). Here, freeze/thaw state represents the transition of Alaskan landscapes

167 from frozen to unfrozen conditions, and does not distinguish between landscape components

168 (soil, vegetation, and snow).

169

170 *Regional GPP and NBP Flux Estimates*

171 Regional GPP is taken from the Polar Vegetation Photosynthesis and Respiration Model

172 (PVPRM) (Luus & Lin, 2015a). PVPRM is a functional representation of ecosystem C fluxes

173 parameterized using eddy covariance data for seven arctic and boreal vegetation types; it is

174 applied regionally and temporally using monthly GOME-2 SIF and North American Regional

175 Reanalysis (NARR) meteorology to obtain three hourly GPP, TER, and NBP at 1/6° latitude x

176 ¼° longitude in Alaska. Phenology is driven by SIF from the Global Ozone Monitoring

177 Experiment (GOME-2) satellite (Joiner et al., 2014; Luus et al., 2017). GOME-2 SIF at 740 nm

178 is derived using a statistically based retrieval, which optimizes model parameters for atmospheric

179 absorption, surface reflectance, and fluorescence radiance using empirical principal component

180 analysis, to enhance retrieval precision and reduce noise. Cloud screening is applied such that

181 only pixels with cloud fraction less than 40% are retained, removing primarily heavily clouded

182 (overcast) pixels within the 40x80 km GOME-2 footprint. The main effect of the remaining

183 clouds is a shielding effect, which masks a fraction of the observed scene (80% of surface

184 observed for 40% cloud cover and cloud optical thickness up to 10) but does not alter the

185 spectral signature of fluorescence (Joiner et al., 2012; 2014). To alleviate reduced signal-to-noise

186 soundings for low sun angles over snow and other high albedo surfaces in northern high latitude

187 spring, GOME-2 SIF values are additionally screened for solar zenith angles less than 60° and

188 cloud fractions below 20%, aggregated monthly and separately calculated for each vegetation

189 class, then weighted according to component vegetation fractions at each PVPRM pixel (Luus et

190 al., 2017). We refer to SIF driven GPP as PVPRM-SIF GPP. We also compare monthly

191 constrained PVPRM-SIF GPP to 5-day mean SIF (same screening criteria) to assess the impact

192 of monthly aggregation on seasonal transitions.

193 PVPRM NBP in Alaska is further optimized using atmospheric CO_2 vertical profiles obtained in

194 the lower atmosphere across Alaska during the Carbon in the Arctic Reservoirs Vulnerability

195 Experiment (CARVE) (Chang et al., 2014; Commane et al., 2017a). Profiles were acquired from

196 Apr-Nov during CARVE campaigns from 2012–2014, and converted to mass-weighted, column-

197 mean CO_2 mole fraction in the atmospheric residual layer. The NBP optimization approach uses

198 the CARVE Polar Weather Research and Forecasting—Stochastic Time-Inverted Lagrangian

199 Transport (PWRF-STILT) framework (Henderson et al., 2015) to calculate the influence

200 function of land surface fluxes on CARVE profiles. Modeled partial column CO_2 enhancements

201 are obtained by convolving the land surface influence functions with NBP priors from PVPRM,

202 which were aggregated to 0.5° x 0.5° for the CO_2 inversion. For each 2-wk measurement period,

203 additive corrections are made to PVPRM NBP that minimized the differences between modeled

204 and observed column CO_2 enhancements, providing spatially explicit, data-constrained NBP for

205 Alaska for each interval. Initial and final campaign dates varied each year, starting/ending on

206   May 27 / Sep 26 in 2012, April 2 / Oct 26 in 2013, and May 23 / Nov 9 in 2014, with a mean

207   start and end dates on day of year (DOY) 127 and 293. We consider optimized NBP as most

208   valid between mid-May and mid-October, although we note that CO_2 fluxes in Jan-Mar compare

209   well to near surface CO_2 observations at CRV and BRW towers as determined from STILT

210   footprints (Commane et al., 2017a). Additive flux corrections are linearly interpolated between

211   aircraft measurement periods and use PVPRM prior flux for late winter when CARVE flights are

212   not available (Dec-Mar) to obtain regional NBP for Alaska (daily, 0.5°x0.5°). CARVE NBP

213   estimates are denoted as CARVE-Opt (Commane et al., 2017b;

214   https://doi.org/10.3334/ORNLDAAC/1389).

215   Commane et al. (2017a) account for uncertainties in observations, background, transport, and the

216   model prior in CARVE-Opt using restricted maximum likelihood estimation, then generate

217   10,000 realizations of the additive flux correction. The standard deviation produces regionally

218   aggregated errors of ~0.25 gC m^{-2} d^{-1} in spring and 0.50 gC m^{-2} d^{-1} in summer, which translates to

219   a net C uptake onset error of 5-10 days on average (cf Fig. 3, Luus et al., 2017 and Fig. 1,

220   Commane et al., 2017a). We do not explicitly account for these uncertainties in our analysis, but

221   consider this timing error in our qualitative analysis of Alaskan net C uptake onset.

222   We provide an indirectly optimized estimate of TER as the difference between PVPRM-SIF GPP

223   and CARVE-Opt NBP, replacing the unconstrained estimate provided by PVPRM. Given that

224   PVPRM-SIF and CARVE-Opt are directly constrained by observations, we consider TER the

225   more uncertain term in this analysis. Since NBP is a small number that balances larger GPP and

226   TER components, small errors in NBP and GPP could lead to large compensating errors in TER.

227   To reduce these compensating errors, we apply a constraint on the signs of TER and GPP to

228   ensure the estimated TER is physically realistic (Bloom & Williams, 2015), and estimate TER

229   as:

230   TER = NBP*a + GPP*b

231   where a and b reflect a range of possible scale factors based on estimated NBP and GPP

232   normally distributed uncertainties of 50% (1-sigma range of 0.5 – 1.5 for a and b). We then

233   sample 1000 samples of TER vectors, and reject unphysical values (TER < 0).

234   We analyze CARVE-Opt NBP against an ensemble of 3 global inverse estimates constrained

235   against satellite or surface CO_2 observations: (1) NASA Carbon Monitoring System Flux (CMS-

236 Flux) estimation and attribution strategy (Liu et al., 2014, 2017; Ott et al., 2015) constrained by

237 column CO_2 from the Greenhouse gases Observing SATellite (GOSAT) using the v7.3 ACOS

238 retrieval algorithm; (2) CarbonTracker 2016 (CT2016) (Peters et al., 2007, with updates

239 documented at http://carbontracker.noaa.gov) constrained by 124 datasets from a global network

240 of tower, aircraft, and shipboard surface *in situ* CO_2 observations; and (3) Jena CarboScope

241 s04_v4.1 (Jena4.1) (update of Rödenbeck et al, 2003, 2005), constrained by surface observations

242 at 59 sites. All inverse estimates are analyzed for the period 2012-2014.

243 We also analyze simulated GPP and NBP from the CASA-GFED3 model (van der Werf et al.,

244 2010), which is run at 0.5°x0.5° monthly resolution and scaled to 3-hour and 1°x1.25° for CO_2

245 modeling studies (https://nacp-files.nacarbon.org/nacp-kawa-01/). Biomass burning and fuel

246 wood C emissions were estimated by the model on daily and monthly time step. These

247 calculations are driven by analyzed meteorological data (MERRA) from the Goddard Modeling

248 and Assimilation Office from 2003-2016.

249

250 ***Flux Tower Site Description***

251 Data for this study were collected from eight eddy covariance towers across four sites on the

252 North Slope and in Interior Alaska (Fig. 1). Brief site descriptions, including location, years

253 analyzed, and references, are provided in Table 1. Tundra sites consist of five total towers at

254 three sites in the North Slope of Alaska, including one tower each at Atqasuk (ATQ) and Ivotuk

255 (IVO) and three towers at Imnavait Creek Watershed (IMN). Boreal sites include three towers at

256 the Bonanza Creek Experimental Forest (BON) in Interior Alaska. NBP measurements were

257 collected at each of the eight eddy covariance towers for at least one year during the period

258 2012-2014, and partitioned into GPP and TER components using the relation between NBP

259 during the nighttime (PAR < 50 umol m^{-2} s^{-1}) and air temperature (Euskirchen et al., 2017;

260 Reichstein et al., 2005). An additional technique using daytime light partitioning at ATQ and

261 IVO (Lasslop et al., 2010) is analyzed for comparison. All NBP and GPP estimates are processed

262 as half-hourly means, then gap-filled and averaged daily. The data processing methodologies for

263 BON and IMN are described in Euskirchen et al. (2014) and Euskirchen et al. (2017),

264 respectively, and for ATQ and IVO in Goodrich et al. (2016). For each location, we sample

PVPRM-SIF GPP and CARVE-Opt NBP only for years with available eddy covariance data from 2012-2014 (see Table 1).

BON is our most southerly site, consisting of three stations in the boreal peatland lowlands of the Tanana Flats of interior Alaska within 0.5 km of each other (Euskirchen et al., 2014). These sites are ~30 km southeast of Fairbanks and vary in the presence and stability of permafrost. They include a black spruce ecosystem with cold soils and permafrost (BON-Spr), a collapse scar bog representing recent permafrost thaw (BON-Bog), and a rich fen lacking permafrost (BON-Fen). BON-Spr is dominated by mature black spruce trees (*Picea mariana*, ~100 years old), with an understory consisting of shrubs, mosses, grasses, and lichens, and sits on an intact peat plateau that rises ~130 cm from the surrounding landscape. BON-Bog is a circular depression that formed through thermokarst, and contains active thaw margins with significant dieback of *Picea mariana*. BON-Fen is composed of grasses, sedges, and forbs. The sites are in close proximity (<0.5 km), and thus co-located within a single grid box of CARVE-Opt and PVPRM-SIF.

IMN is located in the northern foothills of the Brooks Range in northern Alaska (Euskirchen et al., 2017). The watershed is underlain by continuous permafrost, with predominant soils containing 15–20 cm of organic peat underlain by silt and glacial till. The mean annual air temperature (MAT) from 1988–2007 was -7.4°C and the mean annual precipitation was 318 mm, with about 40% occurring as rain and 60% as snow. The landscape is treeless, located approximately 100 km north from latitudinal treeline. IMN includes three stations across three unique tundra sites, including heath (IMN-Hth), moist acidic tussock (IMN-Tus), and wet sedge (IMN-Sed). These sites are also in close proximity (<0.5 km) and therefore share the same grid box.

IVO is located ~300 km to the south of the Arctic Ocean at the foothills of the Brooks Range, with a MAT and summer precipitation of −8.9°C and 210 mm from 2003-2008. IVO vegetation is dominated by tussock-sedge, dwarf-shrub, and moss tundra, and represents the dominant vegetation type in Alaska (Zona et al., 2016). Tussock tundra on flat ground consists of 57% *E. vaginatum* tussocks, 42% inter-tussock vegetation (dominated by *Sphagnum* moss) and 1% moss-dominated hollows (Davidson et al., 2016). The most northerly site, ATQ, is ~100 km south of the Arctic Ocean. MAT and summer precipitation in ATQ are −10.8°C and 100 mm, respectively, for the 1999 to 2006 period. ATQ vegetation is dominated by tundra sedges,

295 grasses, mosses, and some dwarf shrubs <40 cm tall. Tussock tundra on dry ridges and plateaus

296 comprised 21% *Eriophorum vaginatum* tussocks and 79% inter-tussock areas, which are

297 dominated by moss and evergreen dwarf shrubs (Davidson et al., 2016). ATQ has landcover

298 typical of arctic wetlands (Zona et al., 2016).

299 *Analysis*

300 We analyze the period 2012-2014 in Alaska (58°N-72°N, 140°W-170°W) due to availability of

301 CARVE-Opt data. All regional freeze/thaw, GPP and NBP datasets are aggregated to 0.5°x0.5°,

302 then averaged across years to provide a three-year climatology. This study focuses on

303 climatological spatial patterns over this period, rather than year-specific patterns or interannual

304 variability, to provide a first assessment of thaw-C uptake patterns over Alaska. We define

305 seasonal onset dates for snowmelt, thaw, GPP and net C uptake for each grid point in the

306 climatological mean. We acknowledge our short three year period provides a small sample of

307 northern high latitude springs, but captures a range of variability including an average spring in

308 2012, cool and late spring in 2013, and warm and early spring in 2014 (Davidson et al., 2016;

309 Euskirchen et al, 2014; Cox et al., 2017; Commane et al., 2017a).

310 Primary spring thaw is defined as the first DOY when a 14-day running filter contains at least 13

311 days when the land surface was classified as thawed. This high threshold (13 of 14 days, or 93%)

312 discriminates against early 'false thaws' and extended diurnal thaw-refreeze cycles that

313 characterize the Alaskan spring. Previous work (Kim et al., 2012) demonstrates that even an 80%

314 threshold is insufficiently stringent and defines a growing season start date that is too early.

315 Snow-melt date is identified as a one-time switch indicating wet snow with sensitivity to melt-

316 refreeze cycles minimized. We analyze freeze/thaw date as the primary switch for GPP onset, but

317 provide a brief analysis of snow-melt to provide context for spring respiration. We define the

318 GPP onset date as the mean DOY when GPP is between 10-20% of GPP_{max} for that year,

319 accounting for observation noise and range of transition dates from slow to rapid spring recovery

320 in tundra and boreal ecosystems. We define the net C uptake start as the first DOY when NBP >

321 $0 \text{ gC m}^{-2} \text{ d}^{-1}$.

322 We analyze only grid points with average elevation < 1300 m (no alpine vegetation) and less

323 than 60 days of reported thaw or snow-melt status from January 1 to spring thaw date as

324 identified above. This filter isolates data with smooth seasonal transition between frozen and

11

thawed conditions and clearly demarcated frozen winter soils from thawed summer soils. Results are analyzed separately for individual land cover types from Environmental Protection Agency Level 2 and 3 North America ecoregion maps (Fig. 1; https://www.epa.gov/eco-research/ecoregions), with high elevation pixels masked out in white. The primary land cover types analyzed are tundra and boreal, which are sub-divided into the following geographical sub-regions: Tundra Southwest (includes Seward Peninsula, Subarctic Coastal Plains, and Bristol Bay-Nashugak Lowlands), Tundra North Slope (Arctic Coastal Plain and Arctic Foothills), Tundra Brooks (includes Brooks Range), Boreal Interior in central Alaska (Interior Forested Lowlands, Uplands, and Bottomlands), and Boreal Mountains in southeast Alaska (Interior Highlands and Ogilvie Mountains).

Results

Flux Tower Evaluation

Observationally constrained estimates of seasonal GPP and NBP (PVPRM-SIF and CARVE-Opt, respectively) are sampled at and compared to eddy covariance towers (for years with available eddy covariance data, Table 1) for individual sites in Fig. S1 and S2, using native optimized grids (PVPRM-SIF: 1/6°x1/4°; CARVE-Opt: 0.5°x0.5°). PVPRM-SIF and eddy covariance GPP show high consistency of seasonal amplitude, including decreasing amplitude moving north from southern boreal (BON) to northern tundra (IMN, IVO). The high spatial resolution of PVPRM-SIF resolves spatial gradients across diverse landscapes including low GPP (relative to surrounding pixels) at BON and relatively high GPP at IMN (Fig. S3). PVPRM-SIF overestimates growing season GPP at the northern most site (ATQ, Fig. S1H) by a factor of 2-3 depending on partitioning technique (larger error using daytime partitioning at IVO and ATQ). We note a possible calibration bias at ATQ linked to PVPRM model parameter calibration against 2005 ATQ data (Luus et al., 2015; evidence supporting this claim provided in Discussion). We find consistency in the seasonal phase, including timing of GPP onset, at all tundra sites (IMN, IVO, and ATQ), but delayed GPP onset in the lowland boreal landscapes at the BON towers (Fig. S1 A-C). At the BON towers and especially BON-Spr, eddy covariance GPP onset occurs ~1 month earlier than estimated by PVPRM-SIF or implied by GOME-2 SIF retrievals sampled at each site.

354   CARVE-Opt NBP is less consistent with eddy covariance data (Fig. S2). Seasonal amplitude is

355   overestimated at BON boreal sites, underestimated at IMN and IVO tundra sites, and

356   overestimated at ATQ tundra. Reduced agreement of CARVE-Opt NBP (relative to GPP) is

357   attributed to spatial aggregation errors, due to regridding of PVPRM NBP from its native grid

358   (1/6°x1/4°) to the coarser 0.5°x0.5° grid used as the CARVE-Opt prior. The effect is seen clearly

359   in maps of PVPRM NBP at native and aggregated resolutions (Fig. S4 and S5, respectively).

360   Finer scale structure is ultimately smoothed out in CARVE-Opt NBP (Fig. S6). As such,

361   sampling NBP at the native resolution produces higher agreement with tower data than prior and

362   optimized NBP at coarser resolution (Fig. S2).

363   Across-site averages of GPP and NBP for combined tundra (IMN, IVO, ATQ) and boreal (BON)

364   sites are shown in Fig. 2. Here, PVPRM-SIF GPP and CARVE-Opt NPB are sampled at the eddy

365   covariance tower. Spatial averaging improves the NBP comparison at all sites, but especially at

366   IVO and IMN, which exhibit strong gradients of increasing NBP to the south. Estimates of the

367   onset date for GPP and net C uptake are within range of eddy covariance observations at tundra

368   sites, but one month late at BON. Tundra GPP onset is identical (DOY 155), while CARVE-Opt

369   net C uptake is only 6 days late (DOY 170 vs 164) despite a larger net C source through late

370   spring. Boreal GPP onset is 32 days late (DOY 136 vs 104) and net C uptake 25 days late (DOY

371   153 vs 128). GOME2-SIF shows earlier recovery than PVPRM-SIF, but the initial onset is still

372   later than in eddy covariance data. Thaw onset (from AMSR-E and SSM/I) occurs on average on

373   DOY 102 at BON and DOY 130 at tundra sites.

374   Overall, flux towers and observationally constrained estimates show consistent patterns of C flux

375   onset when averaged across boreal and tundra locations. This includes earlier onset of GPP and

376   net C uptake at our boreal location, and lag times of ~4 weeks between thaw and GPP onset at

377   tundra locations. We also find consistent time lags between onset of GPP and net C uptake, with

378   shorter lags in tundra (15 vs 9 days for observationally constrained and eddy covariance

379   estimates, respectively) and longer lags for boreal (17 vs 24 days).

380   Focusing on the relative time lag between thaw and GPP onset shows very different patterns in

381   boreal vs tundra; PVPRM-SIF shows similar time lags in boreal and tundra locations (~33 days),

382   whereas flux towers show no lag in boreal forests but a 33 day lag in tundra. These discrepancies

383   are attributed primarily to late GPP onset bias in PVPRM-SIF in boreal forests, which is linked

384   to   late morning GOME-2 SIF snapshots and thus unresolved diurnal photosynthetic signals in

385   evergreens (e.g., Fig. S7). We elaborate on these discrepancies in the Discussion. Regional

386   patterns of thaw and onset of GPP and net C uptake are examined in more detail below.

Regional Analysis

388   In contrast to eddy covariance data, regional analysis indicates a systematic pattern of reduced

389   time until GPP onset for later thaw dates. Fig. 3a-c shows spatial gradients of spring onset dates

390   for thaw, GPP, and net C uptake. Mean onset dates for boreal and tundra regions are summarized

391   in Table 2. The spatial pattern is characterized by early thaw, GPP onset, and net C uptake in

392   boreal forests (DOY 111±7, 141±5, 145±10 days in the 2012-2014 average, respectively), and

393   delayed onset in tundra (DOY 127±10, 151±5, 163±10 days, respectively), consistent with

394   warmer southern boreal climate and cooler northern tundra climate. Uncertainty is estimated here

395   as sample uncertainties (standard deviation), with random errors in CARVE-Opt (~5 days) added

396   to net C uptake date using sum of errors. Sub-regional variability is negligible in boreal forests,

397   which is clumped in the interior and southeast, and strongly latitude dependent in tundra, which

398   ranges from southwest to northern Alaska. In tundra, thaw (DOY 119±15, 126±5, 133±5), GPP

399   onset (DOY 146±6, 150±3, 153±3), and net C uptake (DOY 159±11, 161±8, 168±9) become

400   later moving north from Tundra Southwest, Brooks, and North Slope sub-regions.

401   While thaw and GPP onset dates are later in tundra compared to boreal regions, the lag time

402   between thaw and GPP onset (Fig. 3d) decreases slightly across the same regions. Lag times

403   range from 40 days in the southern mountains (Alaska Range and Alaska Peninsula Mountains)

404   to ~10 days along the west and north coast (Seward Peninsula and Arctic Coastal Plain), and

405   correspond to average lag times of 29±6 days in boreal regions and 23±7 days in tundra. We also

406   find a high correlation between thaw and GPP onset ($R^2 = 0.69$; p-value < 0.001) with slope less

407   than one ($DOY_{thaw} = 0.5*DOY_{GPP} + 79.5$, where DOY_{thaw} and DOY_{GPP} denote dates of thaw and

408   GPP onset) and consistency across ecoregions (Fig. 4a). Seasonal change in incident shortwave

409   radiation (derived from NCEP2 downwelling shortwave), which increases later in spring moving

410   north, is consistent with the spatial pattern of GPP onset, but shows weaker grid scale correlation

411   with GPP onset compared to thaw onset. We test this by regressing GPP onset against two

412   shortwave onset metrics: (1) shortwave at the time of thaw onset, and (2) onset date of shortwave

413   (10-20% of its annual peak). This analysis yields $R^2 = 0.30$ and 0.31, respectively, representing

weak correlations compared to thaw onset ($R^2 = 0.69$). Furthermore, high latitude tundra receives higher radiation levels at thaw onset than forests to the south; on average, incident radiation along the North Slope exceeds Boreal Interior values by 20% (290 ± 25 vs 241 ± 26 Wm^{-2}) due to later tundra thaw onset (DOY = 133 vs 110). The convergence of soil thawing and seasonal phenology with latitude suggest that tundra ecosystems are well adapted to take advantage of this extra light within 2-4 weeks of thaw onset (more detail on physiological mechanisms in Discussion).

The magnitude of spring GPP and NBP also decrease with later thaw date, but their relationship to each other is ecosystem dependent (Fig. 4b-d). We analyze GPP sensitivity during the one month period from May 15 to June 15, following earliest ecosystem mean GPP onset (DOY 136 in Boreal Interior). May 15 also roughly corresponds to the mean date of first CARVE CO_2 observations (DOY 128), ensuring that CARVE-Opt NBP results are consistent with available spring observations. Mean spring GPP decreases at a rate of -0.8 ± 0.03 gC m^{-2} for every 2 weeks of delayed thaw ($R^2=0.44$). All ecosystems exhibit similar relationships, but the sensitivity of reduced GPP to delayed thaw date is three times stronger on average in boreal forests (e.g., -0.9 ± 0.09 gC m^{-2} d^{-1} per 2 weeks) than in tundra (e.g., -0.3 ± 0.04 gC m^{-2} d^{-1} per 2 weeks). Spring NBP also decreases with later thaw (-0.5 ± 0.02 gC m^{-2} d^{-1}, Fig. 4c), but shows higher consistency (within a factor of 2 difference) across ecosystems (tundra = -0.2 ± 0.06 gC m^{-2} d^{-1}; boreal = $-0.4\pm$ 0.04 g C m^{-2} d^{-1}). As such, the sensitivities of GPP and NBP to thaw in tundra are of similar magnitude while sensitivities for boreal forest are 2-3 times weaker for NBP than GPP. The relationship between spring GPP and NBP for tundra and boreal ecosystems is summarized in Fig. 4d. Overall, NBP increases at half the rate of GPP (y=-0.5x+0.5), but with higher overall sensitivity in tundra (-0.7 ± 0.09) than boreal (-0.35 ± 0.02), and reduced sensitivity for lower GPP (tundra=-0.6 ± 0.1; boreal=-0.5 ± 0.1).

The reduced sensitivity of NBP to GPP in boreal points to TER onset as a key factor also driven by thawing, and which offsets the initial spring GPP. Aggregated plots of TER (Fig. 5a) show an initial increase between snowmelt and landscape thaw (DOY 100 ± 10 and 111 ± 7, respectively), ~4 weeks prior to GPP onset (DOY 141 ± 5). The transition from onset of GPP to net C uptake (DOY 145 ± 10) is short throughout boreal forests (Fig. 3f), but the C uptake rate is initially slow (-1.2 gC m^{-2} month^{-1}) due to synchronous increases in GPP and TER following GPP onset. C

444   uptake accelerates in early June as respiration levels off with substrate depletion and GPP fully

445   recovers from winter.

446   Regional mean onset dates for boreal GPP (DOY 141±5) and net C uptake (DOY 145±10) are

447   early, and corresponding lag time (4±7 das) short, compared to eddy covariance observations at

448   BOR (DOY 104 and 128, and 24 day lag, respectively). However, the lag time is highly variable

449   at regional scale (±7 days). Further, the lag time sampled at the tower (17 days) corresponds

450   more closely with eddy covariance data (20 days). This suggests that the dynamics driving net C

451   uptake onset are not well captured by CARVE-Opt at BOR and potentially other boreal

452   locations, due to sparse airborne CO_2 coverage before mid-May and coarse spatial resolution of

453   CARVE-Opt. Enhanced airborne sampling in after mid-May leads to improved representation of

454   the transition from GPP to net C uptake onset.

455   Respiration offsets an even larger fraction of spring GPP in tundra (Fig. 5b) due to early

456   respiration in mid-April (similar timing to boreal) and delayed GPP onset (10 days later than

457   boreal). The timing of TER onset corresponds closer to the mean onset date of snowmelt (DOY

458   112±12) than landscape thaw (DOY 127±10), consistent with onset of subnivean respiration. The

459   GPP delay also causes a slight phase shift between GPP and TER seasonal cycles, increasing the

460   transition time from onset of GPP (151±5) to net C uptake (163±10 days) by a factor of 3

461   compared to boreal (13±7 days). Longer transition times are found throughout western and North

462   Slope tundra, with longest times just north of the Brooks Range (Fig. 3f). Consequently, the

463   transition time from thaw to net C uptake is delayed in tundra by 37±9 days (Fig. 3e), similar to

464   the boreal transition (34±9 days), but leads to a 50% higher NBP following the transition to net C

465   uptake (-1.8 gC m^{-2} month^{-1}). Regional mean C flux onset dates and lag times in tundra are

466   consistent and within the uncertainty of eddy covariance data analyzed in this study.

467   ***Analysis Against Other CO_2 Inversion Systems***

468   Our reported spring C uptake patterns are specific to CARVE-Opt, which represents an estimate

469   of Alaskan regional-scale dynamics complementary to global inversions due to the closer

470   proximity of airborne CO_2 measurements to regional flux and the higher resolution of

471   atmospheric transport. Using CARVE-Opt as a benchmark, we compare the timing and depth of

472   spring C uptake to global inverse estimates derived from near-surface CO_2 observations from

473   CT2016 and Jena4.1 (Fig. 5 c-d), which are reported daily, and satellite column data from
474   CMSb7.3 (Fig. 5 e-f), which is reported monthly (15th of month).

475   In boreal forests, global and regional inversions show general agreement of earlier and greater
476   uptake compared to tundra. The inversions also show remarkable agreement in spring net C
477   uptake onset and transition back to net source in fall. Global inversions do not show a boreal
478   respiration pulse as seen in CARVE-Opt in mid-May in the three year average, although Jena4.1
479   does reflect this in individual years. Likewise, the presence of this pulse in CARVE-Opt is
480   predicted by PVPRM in all years but only confirmed by CARVE airborne observations in 2013.
481   The pulse is not detected in eddy covariance data at BON-Spr or BON-Bog, but is observed at
482   BON-Fen (Fig. S2). Thus, the repeatability of this pulse over multiple years and at regional scale
483   is unclear.

484   Jena4.1 estimates a smaller rate and depth of uptake in the early growing season compared to
485   CARVE-Opt and CT2016. The smooth transition from March to July aligns well with BON-Spr
486   but not with BON-Fen or BON-Bog. The small seasonal amplitude in Jena4.1 is likely related to
487   the model prior which, in contrast to both CARVE-Opt and the other global inversions, uses a
488   constant zero prior in place of a modeled prior.

489   The relative seasonal patterns across inversions are similar for tundra, but here we give more
490   weight to CARVE-Opt due to the high agreement in phase and amplitude with eddy covariance
491   data (Fig. 2d). CMSb7.3 and CT2016 capture the depth and rate of spring uptake. The sustained
492   tundra efflux from late April to early June is absent from all methods. The true magnitude of the
493   spring tundra source likely falls somewhere between CARVE-Opt (~0.5 gC m^{-2} d^{-1}) and surface
494   inversions (< 0.1 gC m^{-2} d^{-1}) as suggested by eddy covariance data (~0.25 gC m^{-2} d^{-1}), although
495   we note a stronger pulse at the representative tundra site of IVO (Fig. S2g), which peaks at 0.5
496   gC m^{-2} d^{-1} in mid June. Nevertheless, CT2016 and Jena4.1 capture the delayed timing of spring
497   uptake in tundra. In contrast, CMSb7.3 has a pronounced early spring bias in tundra of ~3 weeks.

498   We investigate the CMSb7.3 spring bias in more detail by comparing posterior and prior NBP.
499   Prior NBP is prescribed from CASA-GFED3, shown in Fig. 5e,f. Seasonal NBP amplitude in
500   CMSb7.3 is much improved compared CASA-GFED3. However, the timing of the spring and
501   fall transitions are generally fixed relative to CASA-GFED3, which is early compared to
502   CARVE-Opt in spring. In contrast, CT2016 shows a shift in both the seasonal amplitude and

503   phase relative to its prior, CASA-GFED4.1. Although CASA-GFED4.1 also has an early bias,

504   CT2016 forces a delay in net C uptake onset in boreal and tundra regions in closer agreement

505   with CARVE-Opt across the range of fossil fuel, ocean, and biosphere priors in the CT2016

506   ensemble. The inversion does not have substantial impact on the seasonal amplitude or duration

507   of drawdown following peak uptake, which is underestimated compared to CARVE-Opt. An

508   explanation of spring timing difference across inverse methods is provided in the Discussion.

509   Finally, we examine the source of the early spring bias in CASA-GFED. Previous analyses of

510   CASA in lower latitude boreal forests characterized GPP as generally well represented in

511   satellite constrained diagnostic models, and that differential phasing of TER with respect to GPP

512   is needed to accurately estimate NBP timing surrounding the growing season peak

513   (Messerschmidt et al., 2013). Our analysis of cold northern boreal and tundra ecosystems

514   suggests the opposite: The timing of spring TER onset is well represented in CASA-GFED,

515   while GPP onset is systematically early in boreal and tundra regions (Fig. 6). In tundra in

516   particular, CASA-GFED predicts an early initial GPP increase in late April, followed by a larger

517   secondary jump in late May which increases more rapidly than suggested by PVPRM-SIF. The

518   timing is exacerbated by use of monthly mean normalized difference vegetation index and

519   APAR in CASA, causing GPP to increase more instantaneously than a monthly interpolated

520   change.

521

522   **Discussion**

523   *Spring Photosynthetic Recovery in Alaska Tundra and Boreal Forests*

524   Our results indicate that the timing and magnitude of spring C fluxes in Alaska are correlated

525   with landscape thaw and ecoregion. Tundra ecosystems thaw on average 2 weeks later than

526   boreal forests, and require less time to transition to GPP onset. This pattern of later thaw and

527   reduced lag time in tundra (23±7 days) compared to boreal forests (29±6 days) is consistent with

528   eddy covariance data for eastern Canada and Sweden (Kim et al., 2012). The short time lag in

529   Alaskan tundra, and especially North Slope tundra (20±5 days), is consistent with data in

530   Siberian tundra showing rapid physiological response to warming and snowmelt, a plausible

531   adaptation of high latitude tundra ecosystems to the short growing season (Arneth et al., 2006).

532   Interior boreal forests, on the other hand, have been found to require at least an extra week to

533   reach 10-20% capacity due to pigment adjustments (e.g., Ottander et al., 1995).

534   In Alaskan tundra, PVPRM-SIF indicates a weak physiological response for the first two weeks

535   after thaw onset followed by a more rapid response, with 15% of peak annual GPP attained after

536   three weeks and peak GPP after eight weeks. Low initial GPP, especially in northern Alaska, is

537   attributed to high radiation exposure with later thaw; incident radiation along the North Slope

538   and Brooks Range exceeds Boreal Interior values by 20% and represents a larger percentage of

539   peak annual radiation (82% vs 67%). This apparent light stress, and subsequent rapid recovery, is

540   supported by evidence from *Sphagnum* moss near Barrow, Alaska, which show low levels of

541   photosynthesis early in the season due to photoinhibition, then development of subsurface moss

542   layers and structural protection from high radiation later in the season, enabling increased

543   photosynthetic capacity with reduced risk of light damage (Zona et al., 2011). High nitrogen (N)

544   availability early in the growing season, driven by decreases in microbial biomass and release of

545   N during snowmelt, provides further stimulus to photosynthesis under snow and following

546   snowmelt (Brooks et al., 1998; Starr and Oberbaur, 2003; Larsen et al., 2007). The convergence

547   of soil thawing and seasonal phenology with latitude thus appears to reflect the efficient

548   adaptation of high latitude shrubby ecosystems to cold, high light, and nutrient rich environments

549   and the need to maximize the number of growing days and soil liquid water availability during

550   the short thaw season.

551   These same factors (warm temperatures and high N availability at thaw onset) also stimulate

552   decomposition of soil organic carbon by microbes, leading to simultaneous increases in soil

553   respiration (Oberbaur et al., 1998; Lafleur et al., 2007). Further, competition for N by plants and

554   microbes leads to a crash ~1 month following snow melt, such that tundra plants become N

555   limited (Larsen et al., 2007). These studies are consistent with our finding of delayed time from

556   GPP onset to net C uptake, roughly 2 weeks (14±8 days) in the Tundra North Slope.

557   Although we estimate a longer time lag in boreal forests on average, we note the difference from

558   tundra is within the statistical uncertainty, thus permitting cases where time lag is reversed and

559   shorter in boreal forests. Evidence from mire (tundra) and pine (boreal) sites in Siberia sharing

560   similar climate indicate a shorter time lag in the pine forest, which exhibits a rapid physiological

561   response to above zero temperature even when there is snow on the ground (Arneth et al., 2006;

562   Eukskirchen et al., 2014). Needleleaf trees such as black spruce at Bonanza Creek show a

563   negative lag (GPP reaches ~15% of peak prior to thaw) triggered by early warming (Fig. S7),

564   with the first non-zero GPP values occurring in the afternoon (12–3 pm), prior to onset of

565   primary thaw, on days with above freezing afternoon air temperature and near or below freezing

566   morning temperature (9am–12pm). This early photosynthesis, at least in evergreens, represents a

567   physiological adaptation to stress when sufficient radiation is already available and absorbed by

568   green needles, and small amounts of plant available liquid water in soils can be transported

569   through xylem in conifers and evaporated through leaf stomata as a cooling mechanism (Ishida et

570   al., 2001). These results suggest that sunlight, air temperature, and xylem flow may be better

571   predictors of photosynthetic onset in evergreens than date of primary thaw. However, we note

572   that weak levels of photosynthesis have been observed during transient freeze/thaw cycles during

573   the spring zero curtain preceding primary thaw (Tanja et al., 2003). Diurnal freeze/thaw data

574   may therefore offer a useful indicator of initial photosynthesis, provided that the resolution is

575   fine enough ($< 10 \text{ km}^2$) to distinguish between vegetation and soil landscape components.

576

577   *Limitations and Uncertainties for SIF and CO_2 Observations*

578   In evaluating PVPRM-SIF and CARVE-Opt C flux patterns against eddy covariance data, we

579   find good representation of tundra C flux seasonality and earlier GPP onset in boreal forests, but

580   a potential late onset bias in the timing of spring onset of GPP and net C uptake in boreal forests.

581   We analyze temperature forcing for a cold bias in PVPRM, which might lead to late GPP onset,

582   but find good agreement to observed temperature at Bonanza Creek (Fig. S9). The following

583   limitations in our use of satellite SIF for constraining spring onset of evergreen photosynthesis

584   provides a more likely explanation: (1) GOME-2 overpass time, (2) assumed SIF-GPP linearity,

585   and (3) monthly aggregation.

586   First and foremost, we note that the GOME-2 SIF late morning overpass in Alaska (~11:30 am)

587   hinders observation of early season peak daytime photosynthesis in high latitude evergreens,

588   which can occur even if morning or daily mean temperatures are below freezing (as discussed

589   above), or under transitional (AM frozen, PM thawed) thaw events (Kim et al., 2012). The

590   switch from negative to positive SIF signals at Bonanza Creek occurs following a significant rise

591   in morning temperature of 3-5°C above freezing and near primary thaw (Fig. S7). As such,

592 PVPRM-SIF is unlikely to capture early GPP onset in boreal evergreen forests when constrained

593 solely by spaceborne spectrometers with morning overpasses. Instruments with midday overpass,

594 such as TROPOMI and OCO-2 (e.g., Guanter et al., 2015), are better suited to capture daytime

595 signals, but inadequate by themselves to detect transitional thaw events, and thus cannot

596 represent true daily mean SIF. OCO-2 also lacks the temporal resolution (16 day repeat cycles)

597 to resolve the spring transition (e.g., Sun et al., 2018). Ideally, a harmonized product combining

598 spatially resolved, polar orbiting instruments with morning (GOME-2, SCIAMACHY) and

599 midday (TROPOMI, OCO-2) is needed.

600 It is important to note, however, that SIF is not as well correlated with photosynthesis during the

601 early growing season when leaf level photochemistry precedes increasing SIF emissions

602 (Springer et al., 2017). In evergreens, the SIF-GPP relation changes seasonally with changes in

603 non-photochemical quenching (NPQ) and shifts in carotenoid pigments during transition seasons

604 (Ottander et al., 1995). Increasing pigmentation in fall functions to shed more absorbed energy as

605 NPQ than SIF over winter months (Ottander et al., 1995, Demmig-Adams and Adams, 1996;

606 Porcar-Castell, 2011; Muller et al., 2001) and in early spring with increasing exposure to harmful

607 radiation (Arneth et al., 2006). Increases in absorbed light and temperature in spring during the

608 cold de-hardening period cause relative declines in carotenoid pigments and increases in

609 chlorophyll concentrations, leading to increasing photosynthetic activity, reduced NPQ, and

610 increased dissipation of absorbed light as SIF (Wong and Gamon, 2015; Springer et al., 2017).

611 The increase in SIF and GPP in evergreens is gradual due to the gradually changing pigment

612 ratios of carotenoids and chlorophyll (Wong and Gamon, 2015). Although a recent analysis of

613 GOME-2 SIF has supported a temperature triggered early onset mechanism at pan-Arctic scale

614 (Walther et al., 2016), our results suggest that true onset may occur several weeks earlier. We

615 thus recommend the use of additional remote sensing indices such as chlorophyll carotenoid

616 index (CCI) and photochemical reflectance index (PRI) with midday and morning SIF to

617 interpret the full dynamical range of photosynthesis during spring onset (Springer et al., 2017).

618 This research has also demonstrated that our method to aggregate GOME-2 SIF retrievals by

619 month and biome class, with linear interpolation between values (Luus et al., 2017), is

620 inadequate to resolve spring transitions at high latitudes. Analysis of 5-day mean SIF retrievals,

621 for example, suggest earlier photosynthetic recovery at BON than in the regional average of

622   Alaskan evergreens (Fig. 2a). Future efforts to reduce these errors and interpret patterns of thaw

623   vs C flux onset requires at a minimum non-linear interpolation methods for monthly SIF, and

624   ideally more spatiotemporal explicit application of satellite SIF data in light use efficiency

625   models. More sustained early season, spatially intensive sampling of airborne CO_2 (Parazoo et

626   al., 2016) and longer-term eddy covariance fluxes and from additional sites in high northern

627   boreal forests is also needed.

628   SIF based GPP onset biases in forests feed into NBP calculations and contribute to errors in

629   seasonal amplitude and timing. NBP optimization by CARVE CO_2 observations alleviate most

630   errors at regional scale, but a few remaining grid scale errors persist at tundra and boreal

631   locations. These are attributed to four key factors. First, as discussed above, is the high spatial

632   variability and biome dependence of net C uptake onset. This has an especially large impact on

633   NBP at tundra sites (IMN, IVO) located along the border of Brooks and North Slope sub-

634   regions. Second is the small sample size of boreal forest sites, represented only by BON-Spr.

635   BON-Spr is also unique in its sudden shift in summer NBP magnitude during the two years of

636   overlap with CARVE-Opt, switching from a large summer sink from 2010-2012 to a small or

637   neutral summer sink from 2013-2016 (Fig. S8). We suspect the reduced summer sink is related

638   to a local respiration source from underlying permafrost and thermokarst near the tower, which is

639   undetected by CARVE flights. Third is the lack of consistent airborne CO_2 flights from early

640   April through late May during the eddy covariance NBP transition. Thus our NBP estimate

641   during this period relies on PVPRM, which estimates a delayed net C uptake onset following late

642   GPP onset. Fourth is the relatively short three year record. Significant natural year-to-year

643   variability in the onset of thaw, phenology, and gross/net C uptake at ecosystem and regional

644   scale is common in Alaska (e.g., Kim et al., 2012; Commane et al, 2017a), and makes it difficult

645   to examine climatological spatial patterns over short records. Although the focus of this research

646   is regional scale and thus limited by data availability, we note that ongoing measurements of

647   satellite SIF and airborne CO_2 from the recent NASA Arctic-Boreal Vulnerability Experiment

648   (ABoVE, https://above.nasa.gov) will provide a longer period of record to analyze interannual

649   variability.

650

651   *Limitations and Uncertainties for Eddy Covariance Observations*

652   We also note the factor of 2-3 overestimation of GPP at ATQ by PVPRM-SIF. This error is

653   attributed to two factors: (1) a calibration/validation inconsistency, with PRVPM parameters

654   calibrated using year-round 2005 ATQ data but validated against 2014 ATQ data, and (2)

655   representativeness of eddy covariance. The first factor would cause a high bias only if GPP and

656   NBP in 2005 were higher than 2014 data shown here. Although 2005 data is not available for

657   comparison, we can infer the tendency of GPP in 2005 vs 2014 using a very simple model of

658   GPP as a function of thawing degree days (TDD), estimated as the sum of the mean daily

659   temperature above 0°C and for which we have site level data available from 2005-2014. This

660   model assumes higher peak GPP for larger TDD. We find a TDD of 650 days in 2005 and 563

661   days in 2014, indicating higher productivity in 2005. Previous work using chamber data shows

662   higher GPP in 2013 than in 2014 at ATQ (Davidson et al., 2016), consistent with higher TDD

663   (720 days). These findings indicate higher GPP in 2005, which supports a calibration bias at

664   ATQ and argues for an updated calibration of PVPRM using the longer record of data at existing

665   eddy covariance towers (Luus et al., 2015) and inclusion of new tundra and boreal towers

666   (http://ameriflux.lbl.gov/data/).

667   With regard to the second factor (representativeness), eddy covariance is the most direct

668   measurement of ecosystem fluxes available, however, several uncertainties should be considered

669   in the interpretation of our results: (1) The tower footprint ($\sim 10^0$ km^2) is large compared to

670   individual tree canopies (< 5 m), making it a challenge to disentangle contributions from

671   different vegetation types and C sources in heterogeneous Alaskan landscapes. For example,

672   moss contributions to total NBP range from 25% to 60% in mixed tundra landscapes (Zona et al.,

673   2011) such as seen at Ivotuk (tussock-sedge, dwarf-shrub, and moss tundra) and Atqasuk (sedge,

674   grass, mosses, and dwarf sedge). At the BON cluster, nearby thermokarst permafrost emissions

675   have a substantial influence of C fluxes observed at BON-Spr (Fig. S8); (2) The tower footprint

676   is much smaller compared to footprints for PVPRM-SIF ($\sim 10^2$ km^2), CARVE-OPT ($\sim 10^3$ km^2),

677   and aggregated SIF soundings ($\sim 10^4$ km^2). Although some effort is made to capture sub-grid

678   variability by combining tower clusters (e.g., IMN, BON) and similar ecosystems (e.g., Fig. 2),

679   and by examining sensitivity to spatial resolution (e.g., Fig. S1), we caution that spatial

680   representativeness issues remain in the flux tower – model comparisons. Airborne eddy

681   covariance surveys provide a viable option to increase footprint size toward regional scale

682   (Wolfe et al., 2017); (3) Flux partitioning of eddy covariance NEE into GPP and TER also

683   carries large uncertainties and can yield very different results depending on method (e.g., Fig.

684   S1). This uncertainty in itself may explained the large time lags between thaw and GPP observed

685   at Bonanza Creek. More work is needed to understand the sensitivity of nighttime vs daytime

686   partitioning techniques in Alaska and impact on GPP seasonal onset/offset and amplitude, in

687   particular as a function of length of day, and to compare flux partitioning algorithms to measured

688   respiration form dark chambers across the Arctic.

689

690   *Implications for Top-Down and Bottom-Up Estimates of Net Carbon Exchange*

691   Our results also indicate similar time lags from thaw to net C uptake onset in tundra and boreal

692   (~5 weeks), such that net C uptake occurs later in tundra, with exact timing depending on

693   vegetation type (wet sedge, heath, tussock) (Fig. S2). Delayed tundra uptake is captured in global

694   inverse models, but with net C uptake onset too early in spring and too shallow in summer.

695   Further assessment of CMSb73, which has the most severe spring timing bias, indicates a link to

696   early net C uptake onset in the CASA-GFED prior, and exacerbated by estimation of monthly

697   scale factors for net exchange and limited seasonal coverage of satellite observations. Since

698   CMSb7.3 and CT2016 share a similar prior in CASA-GFED, we can identify three additional

699   factors contributing to difference in spring timing across inverse methods: (1) observation

700   source, (2) optimization method, indicating the application of scale factor correction to model

701   priors, and (3) optimization window, representing the length of time in which scale factors are

702   estimated in the optimization procedure.

703   Regarding the first factor (observation source), CT2016 assimilates *in situ* data, which have

704   continuous year-round coverage, whereas CMSb7.3 assimilates satellite observations derived

705   from reflected sunlight, which have seasonal dependent coverage over high latitudes. As such,

706   the correction to fluxes occurring during polar winter and during snow cover in spring is minimal

707   in CMSb7.3, especially for North Slope and Brooks tundra. However, the enhanced spatial

708   coverage of GOSAT in summer provides a boost in peak summer uptake compared to CASA-

709   GFED. Combining high latitude flask, airborne, and satellite observations into a consistent

710   global inversion framework will improve seasonal and spatial constraints, and retain the

711   advantage of dense satellite observational coverage in summer.

712   Regarding the second factor (optimization method), Jena4.1 has no prior flux information and

713   thus does not apply scale factor orrection. This flexible approach produces an accurate

714   representation of the seasonal transition in spring and fall, but with a trade-off in seasonal

715   amplitude. CT2016 and CMSb7.3 optimize scale factors for NBP at regional and grid-scale,

716   respectively, as corrections to prior fluxes, and thus are more strongly weighted by prior

717   information. This less flexible approach produces more accurate representation of seasonal

718   amplitude, but leads to errors in the seasonal transition timing, which is strongly weighted by

719   prior information under reduced observational coverage.

720   Regarding the third factor (optimization window), CMSb7.3 uses a monthly window; CT2016

721   uses a weekly (8 day) window. We propose that the smaller 8 day window allows more

722   flexibility for data assimilation to adjust the spring transition date, which greatly affects the

723   interpretation of seasonal C uptake dynamics. Alternative inverse methods which estimate

724   scaling factors for gross fluxes (Deng et al., 2016) or persistent grid scale biases (Lokupitiya et

725   al., 2008; Parazoo et al., 2012) permit a shift in seasonal NBP phase relative to prior information.

726   Early C uptake bias in CASA-GFED is consistent with CMIP5 model estimates of seasonal NBP

727   in Alaska, which predict spring net C uptake onset to occur by an average of 18 days earlier than

728   estimated by CARVE-Opt, with 7 of 10 models showing early bias exceeding 15 days, and three

729   models showing a bias exceeding one month (Commane et al., 2017a). In attributing the early C

730   uptake bias, our analysis of GPP and TER fluxes in CASA-GFED indicates an accurate

731   representation of the timing of TER in spring consistent with subnivean respiration, which is

732   simulated in CASA-GFED as a function of soil moisture and temperature (Potter et al., 2013)

733   and in PVPRM as a function of soil temperature (Luus & Lin, 2015b). Our results therefore

734   suggest early GPP onset as the primary culprit in tundra ecosystems. Satellite constrained light

735   use efficiency models that prescribe green biomass using reflectance based vegetation indices

736   typically predict earlier GPP onset and larger spring C uptake in cold climate ecosystems

737   compared to the same models constrained by SIF (Luus et al., 2017; Commane et al., 2017a).

738   Prognostic and diagnostic models used in CMIP5, IPCC, and NACP reports also have a well-

739   known early spring GPP bias (Peng et al., 2015), especially for temperatures below freezing

740   (Schaefer et al., 2012). It is critical for these models to account for survival adaptation under

741   repeated exposure to frost, cold, and frozen soils, which limits root uptake of water and stomatal

742   conductance (Strand and Öquist, 1985; Waring and Winner, 1996; Bergh et al., 1998), and

743   allows cold adapted plants to avoid spring frost damage after budburst (Jeong et al., 2012, 2013)

744   and high radiation following snowmelt inhibiting photosynthetic C uptake (Zona et al., 2011),

745   thus delaying or reducing initial GPP. Other factors such as incorrect prescription of plant

746   functional type also have important effects. Some models such as LPJ-GUESS simulates herbs

747   (grasses) as a proxy for tundra vegetation which in reality may consist largely of shrubs. Grasses

748   have a low growing degree day sum threshold for leaf onset and high light use efficiency which

749   may explain early GPP onset in tundra in Earth System Models. The same issue also applies to

750   conifers and diffuse-porous broadleaves, to which most boreal zone broadleaves belong. Our

751   regional and site-level results support low levels of photosynthesis in tundra initially following

752   snowmelt and leaf-out, as well as longer time lag of ~3 weeks for full phenological recovery.

753

754   *Outlook*

755   Climate models disagree on the trajectory of C balance in northern terrestrial ecosystems under

756   future warming. The advance of spring C uptake observed over the past several decades in these

757   ecosystems is a key climate change metric, but subject to high uncertainty in ecosystem model

758   simulations, which systematically predict early growing season onset. Our results point to

759   landscape thawing as a key driver of seasonal C cycle dynamics in cold northern ecosystems, and

760   a likely factor contributing to early spring C flux biases reported in ecosystem models used in

761   IPCC climate assessment reports for projections of future climate. Failure to account for cold

762   season soil and biochemical processes will lead to biased model and empirical-based estimates of

763   pan-Arctic C sinks which produce too strong of biogenic uptake. This would affect estimates of

764   the timing and magnitude of the permafrost C feedback. Next steps are to quantify sensitivity of

765   (1) spring thaw to meteorological inputs and soil physical processes, and (2) GPP onset to

766   biological processes such as dehardening, xylem flow, and budburst.

767   **Acknowledgements**

781

782 **References**

783 Arneth, A., Lloyd, J., Shibistova, O., Sogachev, A., and Kolle, O.: Spring in the boreal
784   environment: Observations on pre- and post-melt energy and co2 fluxes in two central
785   siberian ecosystems, Boreal Environment Research, 11, 311-328, 2006

786 Badeck, F.W., Bondeau, A., Bottcher, K., Doktor, D., Lucht, W., Schaber, J., Sitch, S., 2004.
787   Responses of spring phenology to climate change. New Phytol. 162, 295–309.

788 Barichivich, J., Briffa, K. R., Myneni, R. B., Osborn, T. J., Melvin, T. M., Ciais, P., … Tucker,
789   C. (2013a). Large-scale variations in the vegetation growing season and annual cycle of
790   atmospheric CO2 at high northern latitudes from 1950 to 2011. *Global Change Biology*,
791   *19*(10), 3167–3183. https://doi.org/10.1111/gcb.12283

792 Bergh, J., McMurtrie, R. E., & Linder, S. (1998). Climatic factors controlling the productivity of
793   Norway spruce: A model-based analysis. *Forest Ecology and Management*, *110*(1–3), 127–
794   139. https://doi.org/Doi 10.1016/S0378-1127(98)00280-1

795 Bhatt, U. S., Walker, D. A., Raynolds, M. K., Comiso, J. C., Epstein, H. E., Jia, G., … Webber,
796   P. J. (2010). Circumpolar Arctic tundra vegetation change is linked to sea ice decline. *Earth
797   Interactions*, *14*(8). https://doi.org/10.1175/2010EI315.1

798 Black, T. A., Chen, W. J., Barr, A. G., Arain, M. A., Chen, Z., Nesic, Z., … Yang, P. C. (2000).
799   Increased carbon sequestration by a Boreal deciduous forest in years with a warm spring.
800   *Geophysical Research Letters*, *27*(9), 1271–1274. https://doi.org/10.1029/1999GL011234

801 Bloom, A. A., & Williams, M. (2015). Constraining ecosystem carbon dynamics in a data-
802   limited world: Integrating ecological "common sense" in a model-data fusion framework.
803   *Biogeosciences*, *12*(5), 1299–1315. https://doi.org/10.5194/bg-12-1299-2015

804 Brooks, P. D., Williams, M. W., and Schmidt, S. K., 1998: Inorganic nitrogen and microbial
805   biomass dynamics before and during spring snow-melt. Biogeochemistry, 43: 1–15.

806 Chang, R. Y.-W., Miller, C. E., Dinardo, S. J., Karion, A., Sweeney, C., Daube, B. C., … Wofsy,
807   S. C. (2014). Methane emissions from Alaska in 2012 from CARVE airborne observations.
808   *Proceedings of the National Academy of Sciences of the United States of America*,
809   (September 2012), 2–7. https://doi.org/10.1073/pnas.1412953111

810 Commane, R., Lindaas, J., Benmergui, J., Luus, K. A., Chang, R. Y.-W., Daube, B. C., …
811   Wofsy, S. C. (2017a). Carbon dioxide sources from Alaska driven by increasing early
812   winter respiration from Arctic tundra. *Proceedings of the National Academy of Sciences of
813   the United States of America*, *114*(21). https://doi.org/10.1073/pnas.1618567114

814 Commane, R., J. Benmergui, J.O.W. Lindaas, S. Miller, K.A. Luus, R.Y-W. Chang, B.C. Daube,
815   S. Euskirchen, J. Henderson, A. Karion, J.B. Miller, N.C. Parazoo, J.T. Randerson, C.
816   Sweeney, P. Tans, K. Thoning, S. Veraverbeke, C.E. Miller, and S.C. Wofsy. 2017b.
817   CARVE: Net Ecosystem CO2 Exchange and Regional Carbon Budgets for Alaska, 2012
818   2014. ORNL DAAC, Oak Ridge, Tennessee, USA,
819   https://doi.org/10.3334/ORNLDAAC/1389.

820 Damm, A., Elbers, J., Erler, A., Gioli, B., Hamdi, K., Hutjes, R., … Moersch, A. (2010). Remote
821   sensing of sun-induced fluorescence to improve modeling of diurnal courses of gross
822   primary production (GPP). *Global Change Biology*, *16*(1), 171–186.

823 Davidson, S. J., Sloan, V. L., Phoenix, G. K., Wagner, R., Fisher, J. P., Oechel, W. C., & Zona,
824   D. (2016). Vegetation Type Dominates the Spatial Variability in CH4 Emissions Across
825   Multiple Arctic Tundra Landscapes. *Ecosystems*, *19*(6), 1116–1132.
826   https://doi.org/10.1007/s10021-016-9991-0

827 Demmig-Adams, B.; Adams, W.W. The role of xanthophyll cycle carotenoids in the protection of
828   photosynthesis. Trends Plant Sci. 1996, 1, 21–26.

829 Deng, F., D. B. A. Jones, C. W. O'Dell, R. Nassar, and N. C. Parazoo (2016), Combining
830   GOSAT XCO2 observations over land and ocean to improve regional CO2 flux estimates, J.
831   Geophys. Res. Atmos., 121, 1896–1913, doi:10.1002/2015JD024157.

832 Elmendorf, S. C., Henry, G. H. R., Hollister, R. D., Björk, R. G., Boulanger-Lapointe, N.,
833   Cooper, E. J., … Wipf, S. (2012). Plot-scale evidence of tundra vegetation change and links
834   to recent summer warming. *Nature Climate Change*, *2*(6), 453–457.
835   https://doi.org/10.1038/nclimate1465

836 Ensminger, I., Sveshnikov, D., Campbell, D. A., Funk, C., Jansson, S., Lloyd, J., … Öquist, G.
837   (2004). Intermittent low temperatures constrain spring recovery of photosynthesis in boreal
838   Scots pine forests. *Global Change Biology*, *10*(6), 995–1008.
839   https://doi.org/10.1111/j.1365-2486.2004.00781.x

840 Euskirchen, E. S., Bret-Harte, M. S., Shaver, G. R., Edgar, C. W., & Romanovsky, V. E. (2017).
841   Long-Term Release of Carbon Dioxide from Arctic Tundra Ecosystems in Alaska.
842   *Ecosystems*, *20*(5), 960–974. https://doi.org/10.1007/s10021-016-0085-9

843 Euskirchen, E. S., Edgar, C. W., Turetsky, M. R., Waldrop, M. P., & Harden, J. W. (2014).
844   Differential response of carbon fluxes to climate in three peatland ecosystems that vary in
845   the presence and stability of permafrost. *Journal of Geophysical Research G:*
846   *Biogeosciences*, *119*(8), 1576–1595. https://doi.org/10.1002/2014JG002683

847 Fleischer, K., Wårlind, D., Van Der Molen, M. K., Rebel, K. T., Arneth, A., Erisman, J. W., …
848   Dolman, A. J. (2015). Low historical nitrogen deposition effect on carbon sequestration in
849   the boreal zone. *Journal of Geophysical Research G: Biogeosciences*, *120*(12), 2542–2561.
850   https://doi.org/10.1002/2015JG002988

851 Ensminger I, Schmidt L, Lloyd J (2008) Soil temperature and intermittent frost modulate the rate
852   of recovery of photosynthesis in Scots pine under simulated spring conditions. New
853   Phytologist, 177, 428–442.

854 Fisher, J. B. and co-authors (2014) Carbon cycle uncertainty in the Alaskan Arctic.
855   Biogeoscience, 11, 4271-4288.

856 Frankenberg, C., Fisher, J. B., Worden, J., Badgley, G., Saatchi, S. S., Lee, J. E., … Yokota, T.
857   (2011). New global observations of the terrestrial carbon cycle from GOSAT: Patterns of
858   plant fluorescence with gross primary productivity. *Geophysical Research Letters*, *38*(17),
859   1–22. https://doi.org/10.1029/2011GL048738

860 Gonsamo A, Chen JM, Price DT, Kurz WA, Wu C (2012) Land surface phenology from optical
861   satellite measurement and CO2 eddy covariance technique. Journal of Geophysical
862   Research: Biogeosciences, 117, doi: 10.1029/2012JG002070.

863 Goodrich, J. P., Oechel, W. C., Gioli, B., Moreaux, V., Murphy, P. C., Burba, G., & Zona, D.
864   (2016). Impact of different eddy covariance sensors, site set-up, and maintenance on the
865   annual balance of CO2and CH4in the harsh Arctic environment. *Agricultural and Forest*
866   *Meteorology*, *228–229*, 239–251. https://doi.org/10.1016/j.agrformet.2016.07.008

867 Goulden, M. L. (1998). Sensitivity of Boreal Forest Carbon Balance to Soil Thaw. *Science*,
868   *279*(5348), 214–217. https://doi.org/10.1126/science.279.5348.214

869 Graven, H. D., Keeling, R. F., Piper, S. C., Patra, P. K., Stephens, B. B., Wofsy, S. C., … Bent,
870   J. D. (2013). Enhanced seasonal exchange of CO2 by northern ecosystems since 1960.
871   *Science (New York, N.Y.)*, *341*(September), 1085–9.
872   https://doi.org/10.1126/science.1239207.

Griffis TJ, Rouse WR, Waddington JM (2000) Interannual variability of net ecosystem CO_2 exchange at a subarctic fen. *Global Biogeochemical Cycles*, **14**, 1109–1121.

Guanter, L., Aben, I., Tol, P. et al. (2015) Potential of the TROPOspheric Monitoring Instrument (TROPOMI) onboard the Sentinel-5 Precursor for the monitoring of terrestrial chlorophyll fluorescence, Atmos. Meas. Tech., 8, 1337-1352.

Harazono Y, Mano M, Miyata A, Zulueta RC, Oechel WC (2003) Inter-annual carbon dioxide uptake at a wet sedge tundra ecosystem in the Arctic. *Tellus*, **55B**, 215–231.

Henderson, J. M., Eluszkiewicz, J., Mountain, M. E., Nehrkorn, T., Chang, R. Y. W., Karion, A., … Miller, C. E. (2015). Atmospheric transport simulations in support of the Carbon in Arctic Reservoirs Vulnerability Experiment (CARVE). *Atmospheric Chemistry and Physics*, *15*(8), 4093–4116. https://doi.org/10.5194/acp-15-4093-2015

Hinzman, L. D., Deal, C. J., Mcguire, A. D., Mernild, S. H., Polyakov, I. V., & Walsh, J. E. (2013). Trajectory of the Arctic as an integrated system. *Ecological Applications*, *23*(8), 1837–1868. https://doi.org/10.1890/11-1498.1

Hugelius G, Strauss J, Zubrzycki S et al. (2014) Estimated stocks of circumpolar permafrost carbon with quantified uncertainty ranges and identified data gaps. Biogeosciences, 11, 6573-6593.

Jafarov, E., & Schaefer, K. (2016). The importance of a surface organic layer in simulating permafrost thermal and carbon dynamics. *Cryosphere*, *10*(1), 465–475. https://doi.org/10.5194/tc-10-465-2016

Jarvis, P., & Linder, S. (2000). Constraints to growth of boreal forests. *Nature*, *405*(6789), 904–905. https://doi.org/10.1002/(SICI)1097-0177(199909)216:1<1::AID-DVDY1>3.0.CO;2-T

Jeong, S. J., Schimel, D., Frankenberg, C., Drewry, D. T., Fisher, J. B., Verma, M., … Joiner, J. (2017). Application of satellite solar-induced chlorophyll fluorescence to understanding large-scale variations in vegetation phenology and function over northern high latitude forests. *Remote Sensing of Environment*. https://doi.org/10.1016/j.rse.2016.11.021

Jeong, S., Medvigy, D., Shevliakova, E., & Malyshev, S. (2012). Uncertainties in terrestrial carbon budgets related to spring phenology, *117*(March), 1–17. https://doi.org/10.1029/2011JG001868

Jeong, S., Medvigy, D., Shevliakova, E., & Malyshev, S. (2013). Predicting changes in temperate forest budburst using continental-scale observations and models, *40*(December 2012), 1–6. https://doi.org/10.1029/2012GL054431

Joiner, J., Yoshida, Y, Vasilkov, A.P., Schaefer, K., Jung, M. (2014). The seasonal cycle of satellite chlorophyll fluorescence observations and its relationship to vegetation phenology and ecosystem atmosphere carbon exchange, Remote Sens. Environ., 152, 375-391.

Jonsson AM, Eklundh L, Hellstr€om M, B€arring L, J€onsson P (2010) Annual changes in MODIS vegetation indices of Swedish coniferous forests in relation to snow dynamics and tree phenology. Remote Sensing of Environment, 114, 2719–2730.

Kim, Y., Kimball, J. S., Zhang, K., Didan, K., Velicogna, I., & McDonald, K. C. (2014). Attribution of divergent northern vegetation growth responses to lengthening non-frozen seasons using satellite optical-NIR and microwave remote sensing. *International Journal of Remote Sensing*, *35*(10), 3700–3721. https://doi.org/10.1080/01431161.2014.915595

Kim, Y., Kimball, J. S., Zhang, K., & McDonald, K. C. (2012). Satellite detection of increasing Northern Hemisphere non-frozen seasons from 1979 to 2008: Implications for regional vegetation growth. *Remote Sensing of Environment*, *121*, 472–487. https://doi.org/10.1016/j.rse.2012.02.014

Lafleur, P. M., and E. R. Humphreys. 2007. Spring warming and carbon dioxide exchange over low Arctic tundra in central Canada. Global Change Biology 14:740–756.

Lasslop, G., Reichstein, M., Papale, D., Richardson, A., Arneth, A., Barr, A., … Wohlfahrt, G. (2010). Separation of net ecosystem exchange into assimilation and respiration using a light response curve approach: Critical issues and global evaluation. *Global Change Biology*, *16*(1), 187–208. https://doi.org/10.1111/j.1365-2486.2009.02041.x

Lawrence, D. M., & Slater, A. G. (2010). The contribution of snow condition trends to future ground climate. *Climate Dynamics*, *34*(7), 969–981. https://doi.org/10.1007/s00382-009-0537-4

Lawrence, D. M., Slater, A. G., Romanovsky, V. E., & Nicolsky, D. J. (2008). Sensitivity of a model projection of near-surface permafrost degradation to soil column depth and representation of soil organic matter. *Journal of Geophysical Research: Earth Surface*, *113*(2). https://doi.org/10.1029/2007JF000883

Lawrence, D. M., Slater, A. G., & Swenson, S. C. (2012). Simulation of present-day and future permafrost and seasonally frozen ground conditions in CCSM4. *Journal of Climate*, *25*(7), 2207–2225. https://doi.org/10.1175/JCLI-D-11-00334.1

Lead, C., Oleson, K. W., Lawrence, D. M., Authors, L., Bonan, G. B., Drewniak, B., … Yang, Z.-L. (2013). Technical Description of version 4.5 of the Community Land Model (CLM). Retrieved from http://library.ucar.edu/research/publish-technote

Liu, J., Bowman, K. W., Lee, M., Henze, D. K., Bousserez, N., Brix, H., … Nassar, R. (2014). Carbon monitoring system flux estimation and attribution: Impact of ACOS-GOSAT XCO2 sampling on the inference of terrestrial biospheric sources and sinks. *Tellus, Series B: Chemical and Physical Meteorology*, *66*(1), 1–18. https://doi.org/10.3402/tellusb.v66.22486

Liu, J., Bowman, K. W., Schimel, D. S., Parazoo, N. C., Jiang, Z., Lee, M., … Eldering, A. (2017). Contrasting carbon cycle responses of the tropical continents to the 2015–2016 El Niño. *Science*, *358*(6360). https://doi.org/10.1126/science.aam5690

Lokupitiya, R. S., Zupanski, D., Denning, A. S., Kawa, S. R., Gurney, K. R., and Zupanski, M. (2008) Estimation of global CO2 fluxes at regional scale using the maximum likelihood ensemble filter, J. Geophys. Res., 113, D20110, doi:10.1029/2007JD009679.

Luus, K. A., & Lin, J. C. (2015a). The Polar Vegetation Photosynthesis and Respiration Model: A parsimonious, satellite-data-driven model of high-latitude CO2 exchange. *Geoscientific Model Development*, *8*(8), 2655–2674. https://doi.org/10.5194/gmd-8-2655-2015

Luus, K. A., & Lin, J. C. (2015b). The Polar Vegetation Photosynthesis and Respiration Model: A parsimonious, satellite-data-driven model of high-latitude CO2 exchange. *Geoscientific Model Development*. https://doi.org/10.5194/gmd-8-2655-2015

McGuire, A. D., Christensen, T. R., Hayes, D., Heroult, A., Euskirchen, E., Kimball, J. S., … Yi, Y. (2012). An assessment of the carbon balance of Arctic tundra: Comparisons among observations, process models, and atmospheric inversions. *Biogeosciences*, *9*(8), 3185–3204. https://doi.org/10.5194/bg-9-3185-2012

Messerschmidt, J., Parazoo, N., Wunch, D., Deutscher, N. M., Roehl, C., Warneke, T., & Wennberg, P. O. (2013). Evaluation of seasonal atmosphere-biosphere exchange estimations with TCCON measurements. *Atmospheric Chemistry and Physics*, *13*(10), 5103–5115.

Müller, P.; Li, X.P.; Niyogi, K.K. Non-photochemical quenching. A response to excess light energy. Plant Physiol. 2001, 125, 1558–1566.

Natali, S. M., Schuur, E. A. G., & Rubin, R. L. (2012). Increased plant productivity in Alaskan

965   tundra as a result of experimental warming of soil and permafrost. *Journal of Ecology*,
966   *100*(2), 488–498. https://doi.org/10.1111/j.1365-2745.2011.01925.x

967 Oberbaur, S.F., G. Starr, E. W. Pop. 1998. Effects of extended growing season and soil warming
968   on carbon dioxide and methane exchange of tussock tundra in Alaska

969 Ottander C, Campbell D, ∈ Oquist G (1995) Seasonal changes in photosystem II organization
970   and pigment composition in Pinus sylvestris. Planta, 197, 176–183.

971 Parazoo, N. C., A. S. Denning, S. R. Kawa, S. Pawson, and R. Lokupitiya (2012) CO2 flux
972   estimation errors associated with moist atmospheric processes. Atmos. Chem. Phys., 12,
973   6405-6416.

974 Parazoo, N. C., Commane, R., Wofsy, S. C., Koven, C. D., Sweeney, C., Lawrence, D. M., …
975   Miller, C. E. (2016). Detecting regional patterns of changing CO2 flux in Alaska.
976   *Proceedings of the National Academy of Sciences of the United States of America*, *113*(28).
977   https://doi.org/10.1073/pnas.1601085113

978 Peng, S., Ciais, P., Chevallier, F., Peylin, P., Cadule, P., Sitch, S., … Zhao, H. (2015).
979   Benchmarking the seasonal cycle of CO 2 fluxes simulated by terrestrial ecosystem models.
980   Global Biogeochemical Cycles, 29, 46-64, https://doi.org/10.1002/2014GB004931

981 Peters, W., Jacobson, A. R., Sweeney, C., Andrews, A. E., Conway, T. J., Masarie, K., … Tans,
982   P. P. (2007). An atmospheric perspective on North American carbon dioxide exchange :
983   CarbonTracker, (8).

984 Porcar-Castell, A. A high-resolution portrait of the annual dynamics of photochemical and non-
985   photochemical quenching in needles of Pinus sylvestris. Physiol. Plant. 2011, 143, 139–153.

986 Pulliainen, J. and co-authors (2017) Early snowmelt significantly enhances boreal springtime
987   carbon uptake, Proceedings of the National Academy of Science, 114, 42, 11081-11086.

988 Ramage, J.M., B.L. Isacks. 2002. Determination of melt-onset and refreeze timing on southeast
989   Alaskan icefields using SSM/I diurnal amplitude variations. *Annals of*
990   *Glaciology* 34(1):391-398, https://doi.org/10.3189/172756402781817761

991 Reichstein, M., Falge, E., Baldocchi, D., Papale, D., Aubinet, M., Berbigier, P., … Valentini, R.
992   (2005). On the separation of net ecosystem exchange into assimilation and ecosystem
993   respiration: Review and improved algorithm. *Global Change Biology*, *11*(9), 1424–1439.
994   https://doi.org/10.1111/j.1365-2486.2005.001002.x

995 Richardson AD, Braswell BH, Hollinger DY, Jenkins JP, Ollinger SV (2011) Near-surface
996   remote sensing of spatial and temporal variation in canopy phenology. Ecological
997   Applications, 19, 1417–1428.

998 Romanovsky, V. E., & Osterkamp, T. E. (2000). Effects of unfrozen water on heat and mass
999   transport processes in the active layer and permafrost. *Permafrost and Periglacial*
1000   *Processes*, *11*(3), 219–239.

1001 Schaefer, K., & Jafarov, E. (2016). A parameterization of respiration in frozen soils based on
1002   substrate availability. *Biogeosciences*, *13*(7), 1991–2001. https://doi.org/10.5194/bg-13-
1003   1991-2016

1004 Schaefer, K., Schwalm, C. R., Williams, C., Arain, M. A., Barr, A., Chen, J. M., … Zhou, X.
1005   (2012). A model-data comparison of gross primary productivity: Results from the north
1006   American carbon program site synthesis. *Journal of Geophysical Research: Biogeosciences*,
1007   *117*(3), 1–15. https://doi.org/10.1029/2012JG001960

1008 Soukupova J, Csefalvay L, Urban O, Kosvancova M, Marek M, Rascher U, Nedbal L (2008)
1009   Annual variation of the steady-state chlorophyll fluorescence emission of evergreen plants
1010   in temperate zone. Functional Plant Biology, 35, 63–76.

1011 Springer, K. R., R. Wang, J. A. Gamon (2017) Parallel Seasonal Patterns of Photosynthesis,
1012   Fluorescence, and Reflectance Indices in Boreal Trees, Remote Sens. 9, 691,
1013   doi:10.3390/rs9070691

1014 Starr, G., and Oberbauer, S., 2003: Photosynthesis of arcticevergreens under snow: implications
1015   for tundra ecosystem carbon balance. Ecology, 84: 1415–1420.

1016 Steiner, N., & Tedesco, M. (2014). A wavelet melt detection algorithm applied to enhanced-
1017   resolution scatterometer data over Antarctica (2000-2009). The Cryosphere, 8(1), 25,
1018   https://doi.org/10.5194/tc-8-25-2014,

1019 Steiner, N. and McDonald, K.C. and Dinardo, S.J. and Miller, C.E. (2015) Snowmelt and
1020   Surface Freeze/Thaw Timings over Alaska derived from Passive Microwave Observations
1021   using a Wavelet Classifier, AGU Fall Meeting Abstracts

1022 Steiner N., McDonald K.C., and Miller C. (2017a) Snowmelt and Freeze/Thaw Mapping of
1023   Boreal and Arctic Alaska using Wavelet Analysis IEEE Transactions on Geoscience and
1024   Remote Sensing, In-Prep.

1025 Steiner, N., K.C. McDonald, and C.E. Miller. 2017b. CARVE: Daily Thaw State of Boreal and
1026   Arctic Alaska from AMSR-E and SSM/I, 2003-2014. ORNL DAAC, Oak Ridge,
1027   Tennessee, USA. https://doi.org/10.3334/ORNLDAAC/1383

1028 Strand, M., and G. Öquist (1985), Inhibition of photosynthesis by freezing temperatures and high
1029   light levels in cold-acclimated seedlings of Scots pine (Pinus sylvestris): I. Effects on the
1030   light-limited and light-saturated rates of CO2 assimilation, Physiol. Plant., 64, 425–430,
1031   doi:10.1111/j.1399-3054.1985.tb08517.x.

1032 Sun, Y., C. Frankenberg, M. Jung, J. Joiner, L. Guanter, P. Köhler, T. Magney (2018) Overview
1033   of solar-induced fluorescence (SIF) from the Orbiting Carbon Observatory-2: Retrieval,
1034   cross-mission comparison, and global monitoring for GPP, Remote Sensing of
1035   Environment, https://doi.org/10.1016/j.rse.2018.02.016.

1036 Tanja S, Berninger F, Vesala T et al. (2003)Air temperature triggers the recovery of evergreen
1037   boreal forest photosynthesis in spring. Global Change Biology, 9, 1410–1426.

1038 Ueyama M, Iwata H, Harazono Y, Euskirchen ES, Oechel WC, Zona D (2013) Growing season
1039   and spatial variations of carbon fluxes of Arctic and boreal ecosystems in Alaska (USA).
1040   Ecological Applications, 23, 1798-1816.

1041 Walther, S., Voigt, M., Thum, T., Gonsamo, A., Zhang, Y., Köhler, P., … Guanter, L. (2016).
1042   Satellite chlorophyll fluorescence measurements reveal large-scale decoupling of
1043   photosynthesis and greenness dynamics in boreal evergreen forests. *Global Change*
1044   *Biology*, 22(9), 2979–2996. https://doi.org/10.1111/gcb.13200

1045 Walther, S., Voigt, M., Thum, T., Gonsamo, A., Zhang, Y., Köhler, P., … Guanter, L. (2016).
1046   Satellite chlorophyll fluorescence measurements reveal large-scale decoupling of
1047   photosynthesis and greenness dynamics in boreal evergreen forests. *Global Change*
1048   *Biology*. https://doi.org/10.1111/gcb.13200

1049 Waring, R. H., and W. E. Winner (1996), Constraints on terrestrial primary production along the
1050   Pacific Coast of North and South America, in High Latitude Rain Forests and Associated
1051   Ecosystems of the West Coast of the Americas: Climate, Hydrology, Ecology, and
1052   Conservation, edited by R. G. Lawford, P. Alaback, and E. R. Fuentes, pp. 89–102,
1053   Springer-Verlag, New York, doi:10.1007/978-1-4612-3970-3_6.

1054 Wolfe, G. M., Kawa, S. R., Hanisco, T. F., Hannun, R. A., Newman, P. A., Swanson, A., Bailey,
1055   S., Barrick, J., Thornhill, K. L., Diskin, G., DiGangi, J., Nowak, J. B., Sorenson, C., Bland,
1056   G., Yungel, J. K., and Swenson, C. A.: The NASA Carbon Airborne Flux Experiment

1057   (CARAFE): Instrumentation and Methodology, Atmos. Meas. Tech. Discuss.,
1058   https://doi.org/10.5194/amt-2017-398, in review, 2017.

1059   Wong, C. Y. S., & Gamon, J. A. (2015). The photochemical reflectance index provides an
1060   optical indicator of spring photosynthetic activation in evergreen conifers. *New Phytologist*,
1061   *206*(1), 196–208. https://doi.org/10.1111/nph.13251

1062   Yi, S., Wischnewski, K., Langer, M., Muster, S., & Boike, J. (2014). Freeze/thaw processes in
1063   complex permafrost landscapes of northern Siberia simulated using the TEM ecosystem
1064   model: Impact of thermokarst ponds and lakes. *Geoscientific Model Development*, *7*(4),
1065   1671–1689. https://doi.org/10.5194/gmd-7-1671-2014

1066   Zhang, T., & Armstrong, R. L. (2001). Soil freeze/thaw cycles over snow-free land detected by
1067   passive microwave remote sensing. *Geophysical Research Letters*, *28*(5), 763-
1068   766, https://doi.org/10.1029/2000gl011952

1069   Zhang, K., Kimball, J. S., Kim, Y., & Mcdonald, K. C. (2011). Changing freeze-thaw seasons in
1070   northern high latitudes and associated influences on evapotranspiration. *Hydrological*
1071   *Processes*, *25*(26), 4142–4151. https://doi.org/10.1002/hyp.8350

1072   Zona, D., Oechel, W. C., Richards, J. H., Hastings, S., Kopetz, I., Ikawa, H., & Oberbauer, S.
1073   (2011). Light-stress avoidance mechanisms in a Sphagnum-dominated wet coastal Arctic
1074   tundra ecosystem in Alaska. *Ecology*, *92*(3), 633–644. https://doi.org/10.1890/10-0822.1

1075   Zona, D., Beniamigo, G., Commane, R. et al. (2016). Cold season emissions dominate the Arctic
1076   tundra methane budget. PNAS, 133(1), 40-45.

1077

1078

1079

Tables

Table 1. Site Characteristics of Eddy Covariance Flux Towers for Alaska.

| Site Name/ID	Ecosystem / Station ID	Region	Latitude, Longitude	Elevation	Site Years Analyzed	Reference
Bonanza Creek Experimental Forest (BON)	Black Spruce Forest (BON-Spr)	Interior Alaska	64.696°N, 148.323°W	100 m	2012-2013	Euskirchen et al., 2014
	Thermokarst Collapse Scar Bog (BON-Bog)	Interior Alaska	64.695°N, 148.321°W	100 m	2012-2013	Euskirchen et al., 2014
	Rich Fen (BON-Fen)	Interior Alaska	64.703°N, 148.313°W	100 m	2012-2013	Euskirchen et al., 2014
Imnavait Creek Watershed (IMN)	Wet Sedge Tundra (IMN-Sed)	North Slope Alaska	68.606°N, 149.311°W	920 m	2012-2014	Euskirchen et al., 2017
	Moist Acidic Tussock Tundra (IMN-Tus)	North Slope Alaska	68.606°N, 149.304°W	930 m	2012-2014	Euskirchen et al., 2017
	Heath Tundra (IMN-Hth)	North Slope Alaska	68.607°N, 149.296°W	940 m	2012-2014	Euskirchen et al., 2017
Ivotuk (IVO)	Tundra dominated by tussock-sedge, dwarf-shrub, moss	North Slope Alaska	68.486°N, 155.750°W	543 m	2014	Goodrich et al., 2016; Zona et al., 2016
Atqasuk (ATQ)	Tundra dominated by sedge, grass, dwarf shrub	North Slope Alaska	70.469°N, 157.409°W	24 m	2014	Goodrich et al., 2016; Zona et al., 2016

1085 **Table 2**: Mean (± SD) [Min Max] dates (DOY) for regional estimates of spring snow melt,
1086 landscape thaw, GPP onset, C sink onset and mean time lags (days) between thaw and GPP onset
1087 and between thaw and C sink onset. Results are shown at eddy covariance (eddy covariance)
1088 towers (eddy covariance observations shown in parentheses), EPA Level II and III ecoregions
1089 (rows 3-7), and for combined tundra and boreal ecoregions (rows 8-9).

Region	Snow-Melt Date (DOY)	Thaw Date (DOY)	GPP Onset Date (DOY)	C Sink Onset Date (DOY)	Thaw-GPP Lag (Days)	Thaw-C Sink Lag (Days)	GPP – C Sink Lag (Days)
Tundra: IMN-ATQ-IVO	121	122	155 (155)	170 (164)	33 (33)	48 (42)	15 (9)
Boreal: BON	102	104	136 (104)	153 (128)	32 (0)	49 (24)	17 (24)
Tundra North Slope	117 ± 12; [84.2 153]	133 ± 5; [118 148]	154 ± 3; [144 160]	167 ± 9; [147 182]	20 ± 5; [9 31]	36 ± 10; [16 50]	14 ± 8; [2 27]
Tundra Brooks	112 ± 8; [94 127]	126 ± 5; [113 132]	150 ± 3; [142 156]	161 ± 8; [139 180]	24 ± 4; [17 33]	35 ± 7; [16 50]	11 ± 6; [-3 25]
Tundra Southwest	103 ± 12; [77 131]	119 ± 15; [85 135]	146 ± 5; [137 164]	159 ± 11; [139 178]	26 ± 11; [7 57]	41 ± 10; [13 76]	13 ± 8; [-3 36]
Boreal Interior	98 ± 8; [78 121]	110 ± 7; [96 129]	139 ± 3; [135 149]	144 ± 7; [137 175]	29 ± 5; [16 42]	34 ± 6; [16 61]	5 ± 5; [-2 30]
Boreal Mountain	102 ± 11 [66 136]	112 ± 7; [89 152]	142 ± 5; [135 177]	146 ± 12; [133 188]	30 ± 6; [-2 67]	34 ± 11; [5 82]	4 ± 9; [-17 38]
Tundra: North Slope + Brooks + Southwest	112 ± 12; [77 153]	127 ± 10; [85 148]	151 ± 5; [137 164]	163 ± 10; [139 182]	23 ± 7; [7 57]	37 ± 9; [13 76]	13 ± 7; [-3 36]
Boreal: Interior + Mountain	100 ± 10; [66 136]	111 ± 7; [89 152]	141 ± 5; [135 177]	145 ± 10; [133 188]	29 ± 6; [-2 67]	34 ± 9; [5 82]	4 ± 7; [-17 38]

Figures
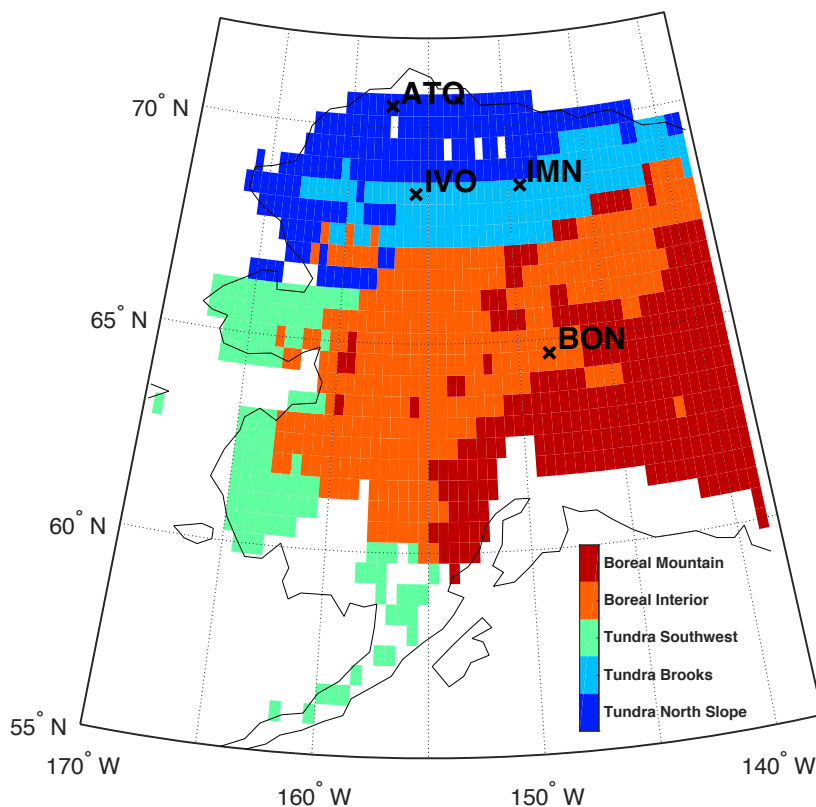
Fig. 1: Map showing spatial pattern of vegetation and location of flux towers. Vegetation is derived from US EPA Level 2 ecoregion maps for boreal (reds) and tundra (blue). Tower sites include: Bonanza Creek (BNZ: 64.70ºN, 148.32ºW), Imnavait (IMN: 68.62ºN, 149.30ºW), Ivotuk (IVO: 68.48ºN, 155.75ºW), and Atqasuk (ATQ: 70.47ºN, 157.40ºW). IMN and BON sites each include three additional eddy covariance stations (see Table 1).
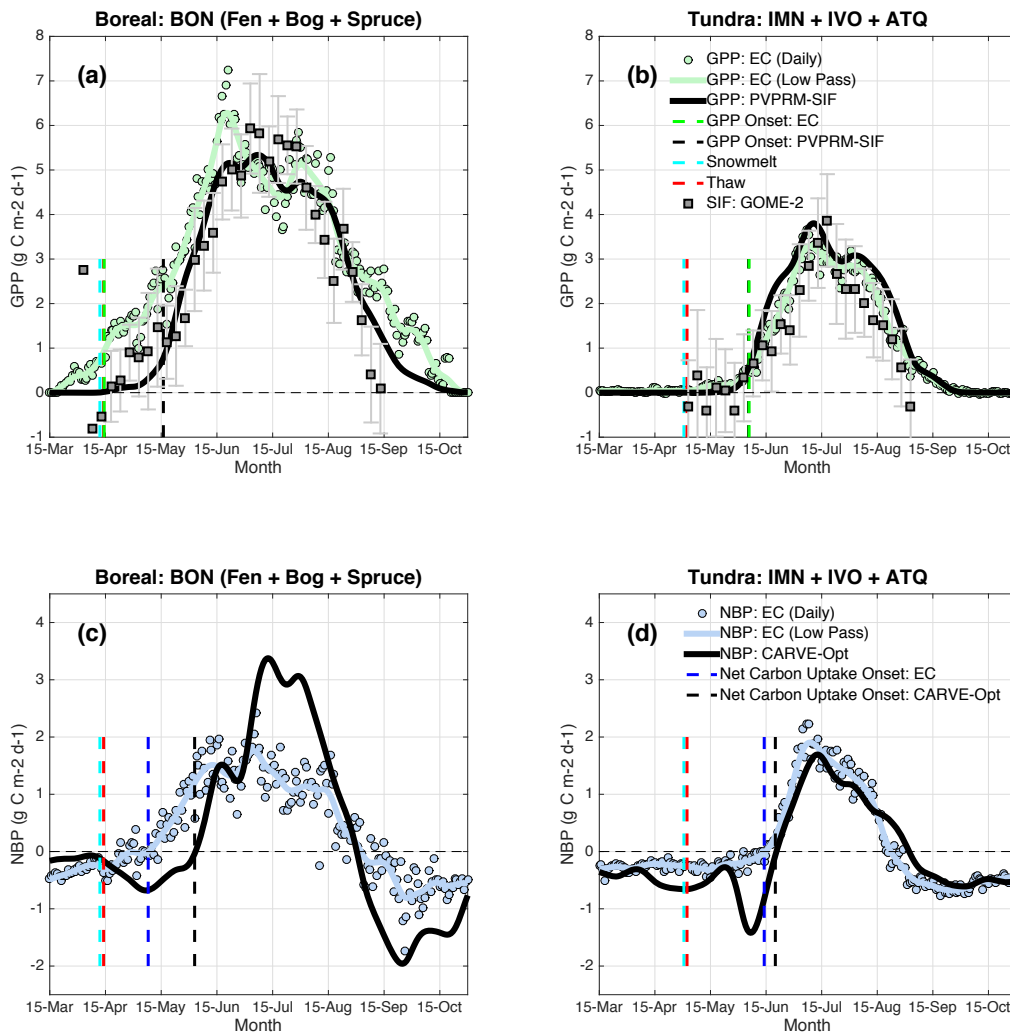
Fig. 2: Evaluation of observationally constrained estimates of seasonal gross primary production (PVPRM-SIF GPP, a-b) and net biome production (CARVE-Opt NBP, c-d) against tower eddy covariance data in interior and northern Alaska, averaged from 2012-2014. Daily averages (symbols) and low pass filters (lines) are shown for flux towers (green = GPP, blue = NBP), and low pass butterworth filters (order 2, cutoff frequency = 0.1) for PVPRM-SIF (solid black, top) and CARVE-Opt (solid black, bottom). Boreal fluxes are averaged over the cluster of Spruce, Fen, and Bog sites at Bonanza Creek Experimental Forest (BON, 3 sites total). Tundra fluxes are averaged over the cluster of Hedge, Sedge, and Tussock sites at IMN and individual sites at IVO and ATQ (five sites total). CARVE-Opt and PVPRM-SIF are sampled at towers only for years

1107   when growing season eddy covariance data is available, which differs between sites (see Table

1108   1). Onset dates for snowmelt, thaw, GPP, and net carbon uptake shown in vertical dashed lines.

1109   5-day mean retrievals of GOME-2 solar induced fluorescence (SIF) and standard error sampled

1110   in a 2º x 2º grid box surrounding eddy covariance tower and normalized by PVPRM-SIF are

1111   shown in grey in A-B. Thaw, GPP, and net C sink onset dates are provided in Table 2. Positive

1112   NBP values denote net sink of atmospheric CO_2. Seasonal C flux dynamics are well represented

1113   by observationally constrained estimates in tundra, but show delayed spring onset compared to

1114   the black spruce forest.
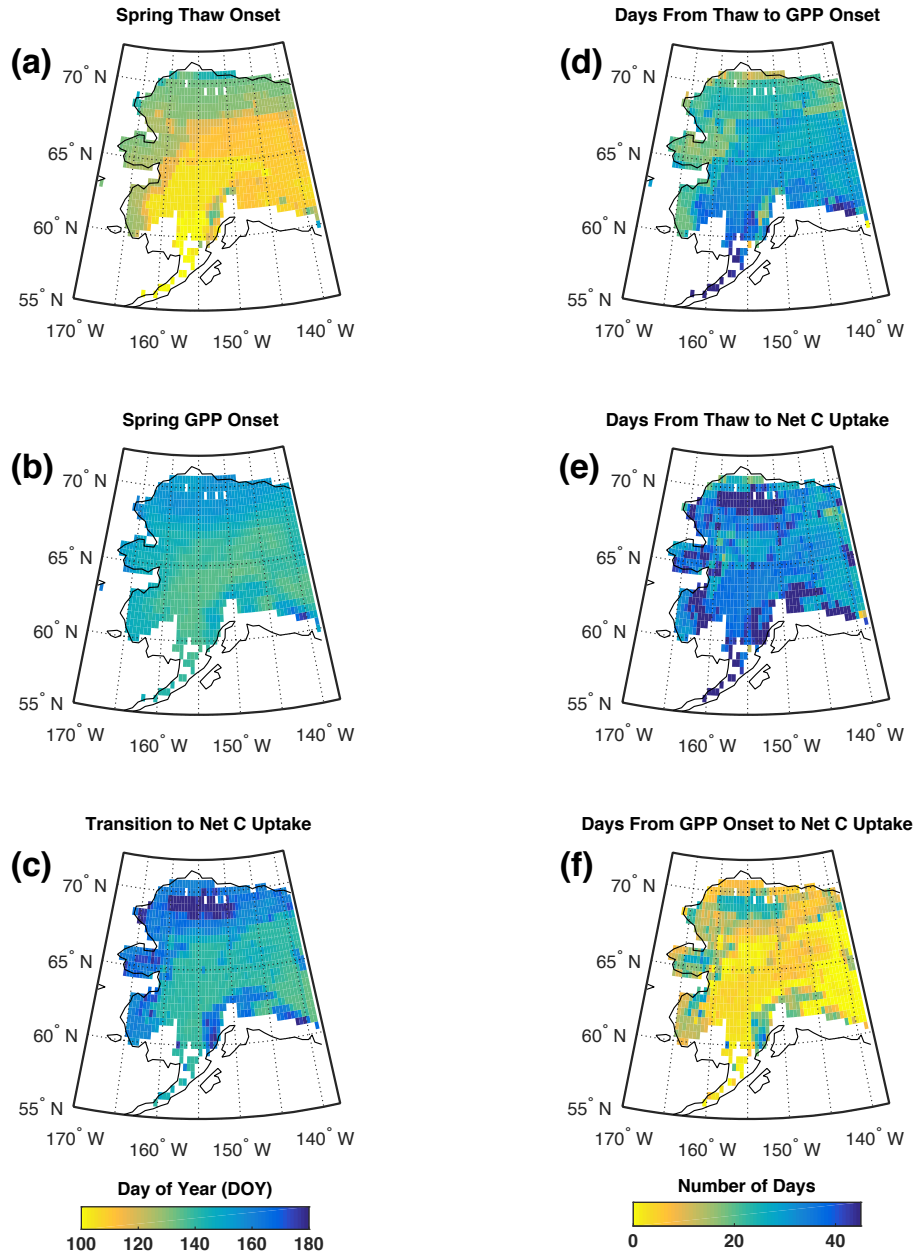
Fig. 3: Maps showing spatial patterns of spring onset dates for landscape thaw, GPP, and net C uptake at regional scale for Alaska. (A) Spring thaw date, representing the transition of the landscape from frozen to thawed conditions, is derived from AMSR-E and SSM/I. (B) Spring GPP onset, representing the date when ecosystem GPP reaches 10% of the growing season peak, is derived from PVPRM-SIF. (C) Net C uptake, representing the spring transition from net C source in winter to net C sink in summer, is derived from CARVE-Opt, a regional flux inversion

1122   for Alaska constrained by airborne CO_2 profiles. Number of days between thaw and GPP onset

1123   (D), thaw and net C uptake (E), and GPP onset to net C uptake (F) are estimated as the difference

1124   between maps in A-C. Values in A-C are plotted as day of year (DOY). This shows similar

1125   spatial patterns of the timing of spring thaw and GPP onset, and a decrease in the number of days

1126   from thaw to spring onset moving from south to north along the boreal-tundra gradient.
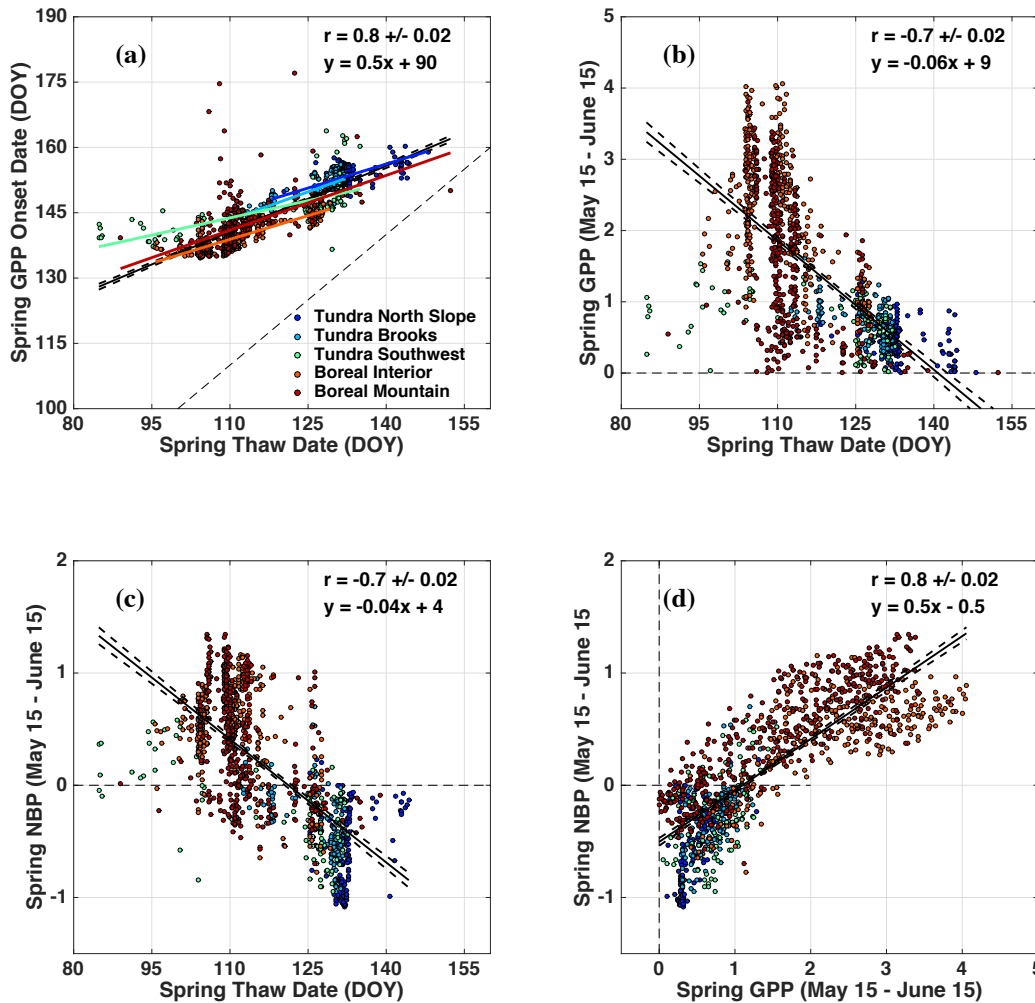
1127

1128   Fig. 4: Relationship between spring CO_2 flux and landscape thaw. Scatter plots show regressions

1129   of (A) Spring GPP onset date vs thaw date, (B) Mean spring GPP from May 15 – June 15 vs

1130   thaw date, (C) Mean spring NBP from May 15 – June 15 vs thaw date, and (D) mean spring NBP

1131   vs GPP (g C m-2 d-1). Positive NBP denotes net C uptake by plants. Colors denote the 5

1132　ecoregions of interest. Regression lines are plotted for each ecoregion in A. Regression statistics

1133　are reported for all points combined in each sub-panel. We note several emergent patterns: (1)

1134　the relationship between dates of spring GPP onset and landscape thaw are consistent across

1135　ecoregions, (2) the magnitude of GPP is more sensitive to thaw date in boreal than tundra, (3)

1136　NBP magnitude is equally sensitive to thaw date in boreal and tundra, and (4) NBP is more

1137　sensitive to GPP change, and hence thaw date, in tundra.
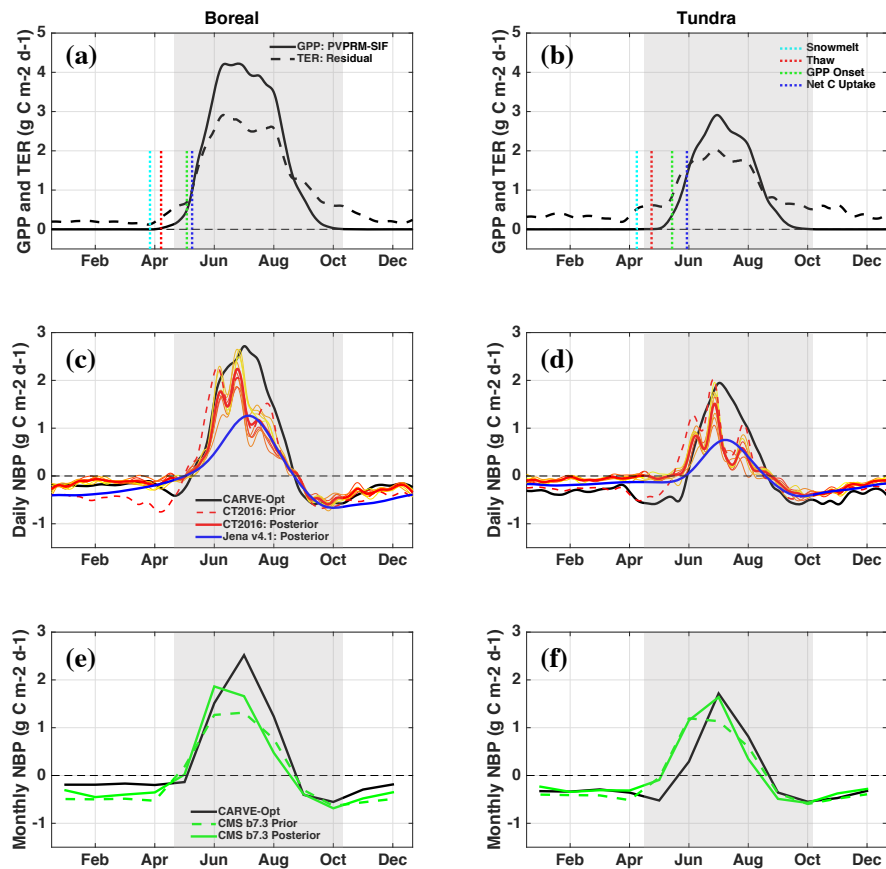
1138

1139　**Fig. 5**: Seasonal GPP and NBP patterns for boreal and tundra ecoregions. (A-B) Seasonal GPP

1140　(solid) from PVPRM-SIF and terrestrial ecosystem respiration (TER, dashed) from the residual

1141　of CARVE-Opt NBP and PVPRM-SIF GPP. (C-D) Seasonal NBP derived from daily averages

1142　of CARVE-Opt (black), CT2016 ensemble (red), and Jena v4.1 (blue) posterior fluxes and

1143　CT2016 prior fluxes (red dashed). (E-F) Seasonal NBP (positive denotes net sink) derived from

1144　monthly averages of CARVE-Opt (black) and CMS b7.3 posterior (green solid) and prior (green

1145   dashed) fluxes. Results for boreal ecoregions shown in the left column, and tundra in the right

1146   column. X-axis labels represent middle of month. Shaded area shows valid range of

1147   climatological CARVE-Opt NBP for the period 2012-2014, representing CARVE campaign start

1148   and end dates (May 7 and Oct 20 on average). Vertical dashed lines denote mean date of snow-

1149   melt (cyan), landscape thaw (red), GPP onset (green), and net C uptake (blue) for each

1150   ecoregion. CT2016 and Jena v4.1 are global inverse estimates derived from near-surface CO_2

1151   observations. CMS b7.3 is derived from satellite column integrated CO_2. CT2016 results are

1152   shown for 8 ensemble runs driven by different combination of fossil fuel, ocean, and biosphere

1153   priors. The results show variable patterns of the amplitude and timing of seasonal CO_2 exchange

1154   for each ecoregion and inversion method.

1155
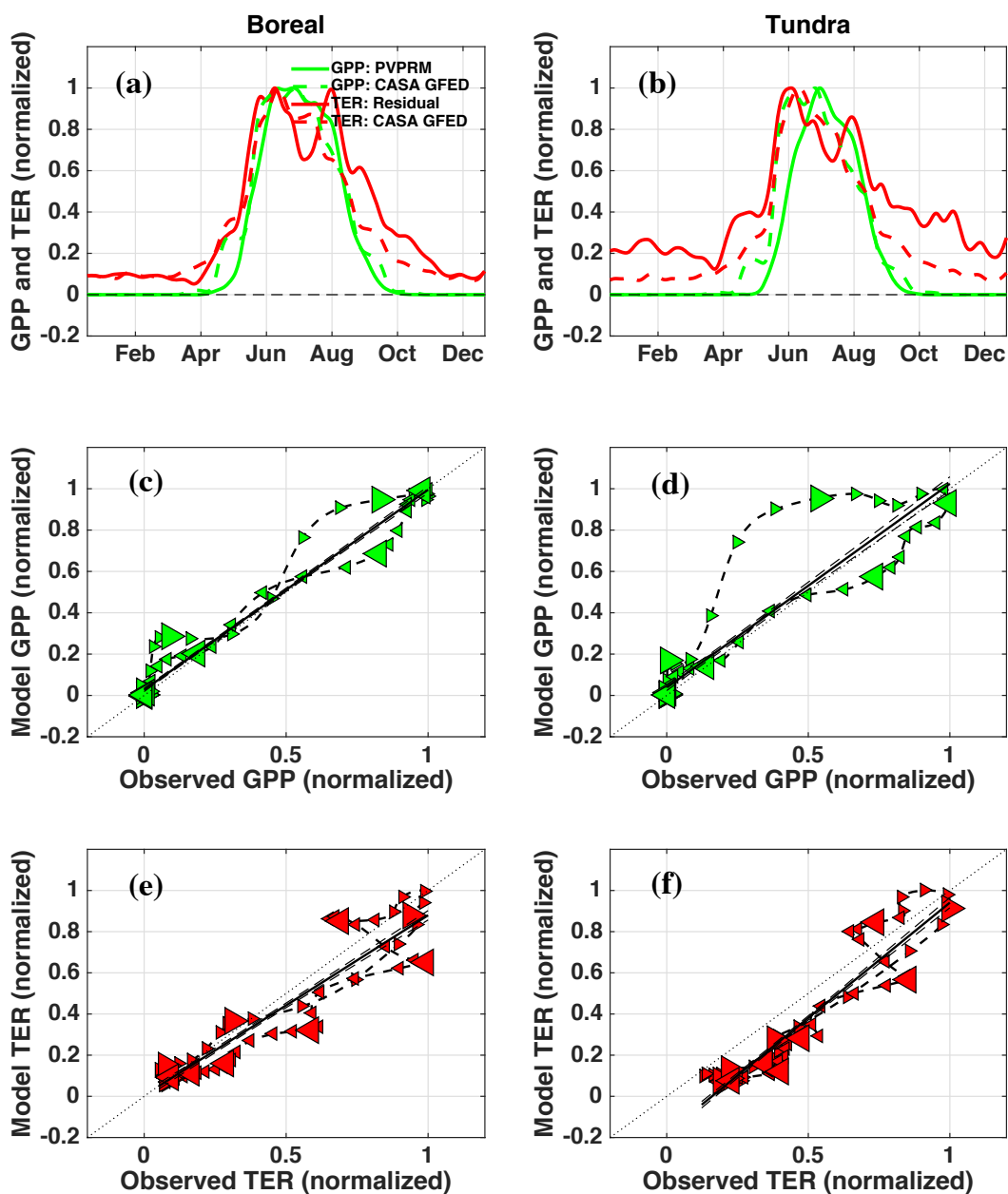
Fig. 6: Errors in predicted seasonal GPP and TER. (A-B) Seasonal time series of daily optimized (solid) and simulated (dashed) GPP (green) and TER (red). (C-D) Regression of simulated and optimized GPP. (E-F) Regression of simulated and optimized TER. Optimized GPP is taken from PVPRM-SIF and TER as the residual of CARVE-Opt NBP and PVPRM-SIF GPP. Values are reported every 5 days, with large symbols denoting mid-month. Model fluxes are taken from

1162   CASA GFED3. The results show a positive bias in spring GPP in boreal and tundra ecosystems,

1163   driven by early GPP onset, which leads to an early transition from net C source to sink compared

1164   to CARVE-Opt.

1165

1166

1167